



EDGEWOOD

CHEMICAL BIOLOGICAL CENTER

U.S. ARMY SOLDIER AND BIOLOGICAL CHEMICAL COMMAND

ECBC-CR-048

**FEASIBILITY STUDY FOR THE MINI-FREQUENCY
AGILE LASER (MFAL) LIDAR SYSTEM**

**David B. Cohn
David Fink
John H. Wang**

**HUGHES AIRCRAFT COMPANY
El Segundo, CA 90245**

Russell E. Warren

**SRI INTERNATIONAL
Menlo Park, CA 94025**

January 2002

**Approved for public release,
distribution is unlimited.**



20020325 175

Aberdeen Proving Ground, MD 21010-5424

Disclaimer

The findings in this report are not to be construed as an official Department of the Army position unless so designated by other authorizing documents.

REPORT DOCUMENTATION PAGE			Form Approved OMB No. 0704-0188
<p>Public reporting burden for this collection of information is estimated to average 1 hour per response, including the time for reviewing instructions, searching existing data sources, gathering and maintaining the data needed, and completing and reviewing the collection of information. Send comments regarding this burden estimate or any other aspect of this collection of information, including suggestions for reducing this burden, to Washington Headquarters Services, Directorate for Information Operations and Reports, 1215 Jefferson Davis Highway, Suite 1204, Arlington, VA 22202-4302, and to the Office of Management and Budget, Paperwork Reduction Project (0704-0188), Washington, DC 20503.</p>			
1. AGENCY USE ONLY (Leave Blank)	2. REPORT DATE	3. REPORT TYPE AND DATES COVERED	
	2002 January	Final; 94 Mar – 96 Jul	
4. TITLE AND SUBTITLE Feasibility Study for the Mini-Frequency Agile Laser (MFAL) LIDAR System			5. FUNDING NUMBERS C-DAAM01-94-C-0076
6. AUTHOR(S) Cohn, David B.; Fink, David; Wang, John H. (Hughes Aircraft Company); and Warren, Russell E. (SRI International)			
7. PERFORMING ORGANIZATION NAME(S) AND ADDRESS(ES) Hughes Aircraft Company, P. O. Box 902, El Segundo, CA 90245 SRI International, Menlo Park, CA 94025			8. PERFORMING ORGANIZATION REPORT NUMBER ECBC-CR-048
9. SPONSORING/MONITORING AGENCY NAME(S) AND ADDRESS(ES) DIR, ECBC,* ATTN: AMSSB-RRT, APG, MD 21010-5424			10. SPONSORING/MONITORING AGENCY REPORT NUMBER
11. SUPPLEMENTARY NOTES COR: Felix Reyes, AMSSB-RRT (410) 671-2140 *When this study was conducted, the U.S. Army Edgewood Chemical Biological Center (ECBC) was known as the U.S. Army Edgewood Research, Development and Engineering Center (ERDEC).			
12a. DISTRIBUTION/AVAILABILITY STATEMENT Approved for public release; distribution is unlimited.		12b. DISTRIBUTION CODE	
<p>13. ABSTRACT (Maximum 200 words)</p> <p>Direct and coherent detection LIDAR systems were analyzed for DISC and DIAL detection of stack and pollutant chemicals. Tradeoffs included output energies of 60 and 120 mJ, powers of 2 and 10 W, and several values of telescope diameter, atmospheric attenuation, and backscatter coefficient. Longer ranges were found with coherent systems. Extrapolation from field data showed that direct detection of stack emissions could be effective up to 5 km. Based on prior laser development and field experience, a conceptual design for a man-portable, direct detection sensor gave a total weight of 33 lb with a length of 15 in., height of 12 in., and width of 6 in. Development of the conceptual design would require low risk application of standard engineering practices. Algorithms were formulated for application to the multi-wavelength data typical of a MiniFAL sensor to circumvent the limitations of the conventional ratio method using two closely spaced wavelengths. The algorithms used the likelihood ratio test methodology of multivariate statistical inference theory and were successfully applied to synthetic and field data. Wavelengths for most of the selected chemicals were identified; and by using wavelength shifting in crystals through nonlinear effects, all remaining chemicals of interest could be detected.</p>			
14. SUBJECT TERMS Carbon Dioxide (CO ₂) laser Differential absorption lidar (DIAL) Transversely Excited Atmospheric (TEA) laser			15. NUMBER OF PAGES 63
			16. PRICE CODE
17. SECURITY CLASSIFICATION OF REPORT UNCLASSIFIED	18. SECURITY CLASSIFICATION OF THIS PAGE UNCLASSIFIED	19. SECURITY CLASSIFICATION OF ABSTRACT UNCLASSIFIED	20. LIMITATION OF ABSTRACT UL

BLANK

PREFACE

The work described in this report was authorized under Contract No. DAAM01-94-C-0076. This work was started in March 1994 and was completed in all technical aspects in July 1996. The report covers all technical efforts and recommendations for further development.

This report contains descriptions of equipment which uses commercially available items. The use of either trade or manufacturers' names in this report does not constitute an official endorsement of any commercial products. This report may not be cited for purposes of advertisement.

This report has been approved for public release. Registered users should request additional copies from the Defense Technical Information Center; unregistered users should direct such requests to the National Technical Information Service.

BLANK

CONTENTS

1. SUMMARY	1
2. INTRODUCTION	3
3. PERFORMANCE ANALYSIS.....	5
3.1. ANALYSIS MATRIX.....	5
3.2. LASER RADAR MODEL.....	6
3.3. ANALYSIS RESULTS.....	8
3.4. RANGE-RESOLVED CONSIDERATIONS.....	13
4. LASER AND SENSOR DESIGN	15
4.1. PRIOR WORK.....	16
4.1.1. Modular TEA laser.....	16
4.1.2. Frequency Agile Laser.....	18
4.1.3. FAL sensor	21
4.2. MINIFAL DESIGN.....	23
4.2.1. Laser	25
4.2.2. Sensor optics.....	26
4.2.3. Electronics.....	26
4.2.4. Weight analysis	27
4.3. MINIFAL DEVELOPMENT.....	29
5. ALGORITHM DEVELOPMENT.....	31
5.1. INTRODUCTION AND SUMMARY	31
5.2. LIKELIHOOD RATIO TEST METHODOLOGY	33
5.3. ALGORITHM CONSTRUCTION.....	34
5.3.1. Uniform spectral background	35
5.3.2. Known spectral background	41
5.3.3. Measured spectral background	44
6. WAVELENGTH SELECTION	50
7. CONCLUSIONS AND RECOMMENDATIONS.....	53
REFERENCES	55

FIGURES

3-1. Laser radar model block diagram.....	7
3-2. Range capability of direct detection topographic DIAL systems.....	9
3-3. Range capability of coherent detection topographic DIAL systems.....	10
3-4. Range capability of direct detection range-resolved system for 1.6 dB/km.....	10
3-5. Range capability of direct range-resolved system for 2.3 dB/km.....	11
3-6. Range capability of coherent range-resolved system for 1.6 dB/km.....	11
3-7. Range capability of coherent range-resolved 2.3 dB/km system.....	12
3-8. Range capability of direct DIAL system with retro.....	12
3-9. Range capability of coherent DIAL system with retro.....	13
3-10. FAL direct detection with range-resolved cloud.....	14
4-1. Modular TEA laser.....	16
4-2. High voltage section.....	17
4-3. Frequency Agile Laser.....	18
4-4. FAL resonator schematic.....	19
4-5. FAL sensor.....	22
4-6. FAL sensor optical schematic.....	22
4-7. MiniFAL conceptual design.....	24
4-8. MiniFAL component layout.....	25
4-9. MiniFAL data acquisition system block diagram.....	27
5-1. Algorithm computation flow diagram.....	32
5-2. Hypothetical absorptivity vs wavelength.....	39
5-3. Estimated CL.....	39
5-4. Synthetic data vs range bin.....	44
5-5. Estimated CL vs range.....	44
5-6. CL for MEK vs test data.....	48
5-7. CL for three material injection.....	49

TABLES

3-1. Performance analysis matrix.....	6
3-2. Direct detection sensor parameters.....	8
3-3. Coherent detection sensor parameters.....	8
3-4. Performance analysis results.....	13
4-1. Modular TEA laser specifications.....	17
4-2. FAL specifications.....	19
4-3. FAL sensor specifications.....	21
4-4. MiniFAL specifications.....	25
4-5. MiniFAL laser weight analysis.....	28
4-6. MiniFAL sensor weight analysis.....	29
4-7. Design validation and component development approaches.....	30
6-1. Sample chemicals and selected wavelengths.....	52

ABBREVIATIONS AND ACRONYMS

ATLAS	Advanced Technology LADAR System
CBDC	Chemical and Biological Defense Command
CL	Concentration-Path Length Product
DIAL	Differential Absorption LIDAR
DISC	Differential Scattering
FAL	Frequency Agile Laser
FLIR	Forward Looking Infrared
FWHM	Full-Width-Half-Maximum
GPS	Global Positioning System
IR	Infrared
IR&D	Independent Research and Development
PC	Personal Computer
PCMCIA	Personal Computer Memory Card International Association
RAS	Remote Active Spectrometer
SPD	Short Pulse Demonstration
SRI	Stanford Research Institute
TEA	Transversely Excited Atmospheric

BLANK

FEASIBILITY STUDY FOR THE MINI-FREQUENCY AGILE LASER (MFAL) LIDAR SYSTEM

1. SUMMARY

The primary purpose of this program was to evaluate the capabilities of DIAL (Differential Absorption LIDAR) and DISC (Differential Scattering) for the detection of stack gas emissions based on the Hughes FAL (Frequency Agile Laser) technology. It was also a goal to design a portable LIDAR system that could reach to ranges of 1-3 km, 3-5 km, and 5-10 km for detection of chemicals of military interest and for civilian environmental monitoring.

Extensive analysis was first performed for both direct and heterodyne detection chemical sensors. This included systems with output energies up to 120 mJ per pulse (direct detection) or cw powers up to 10 W (heterodyne detection), based on typical CO₂ TEA laser and CO₂ waveguide laser technology, respectively. Several promising systems were identified for further study. In the case where the laser beam was reflected off topographic features, the results were not surprising. Sensors using either direct or coherent detection performed reasonably well for 6 in diameter receivers, giving ranges out to 5 km and 8 km for direct and heterodyne detection, respectively. In the case of range-resolved targets, range for direct detection was reduced to about 300 m and to 1.5 km for coherent detection. Importantly, it was found that when the radar model was applied to an extrapolation from actual cloud data with the direct detection system, the predicted range-resolved capability was greatly extended to 5 km. Results in the literature for range-resolved, direct detection of stack emissions supports this contention. It is suggested that the backscatter coefficient for stack emissions is about a factor of 10⁴ higher than the presumed atmospheric backscatter coefficient. Therefore, in the absence of conclusive field data, it appears that both the direct and coherent detection systems can be applied successfully to the detection of stack gas emissions. There are other operational and systems issues that could favor one or the other detection approach.

As a result of the systems analysis, a conceptual design for a miniature CO₂ TEA (Transversely Excited Atmospheric) FAL was formulated. This MiniFAL (Miniature FAL) design is based on hardware development and field experience obtained over the last decade under a Hughes IR&D (Independent Research and Development) program and the FAL program with the U.S. Army CBDC (Chemical and Biological Defense Command). The MiniFAL design effort resulted in a device with an overall length of 14 in, width of 6 in and height of 12 in. Total weight is estimated to be 33 lb, based on detailed analysis of both existing components and component development using standard engineering methods and materials. Development of the MiniFAL requires further development of certain components and subsystems, but it is anticipated that the associated risks will be manageable. The MiniFAL characteristics clearly put it in the category of portability by one person and it is designed to be operated by a single person.

In the development of an algorithm for the MiniFAL mission, it was recognized that the conventional method of chemical detection using two closely spaced wavelengths was not sufficient. The crucial assumption underlying two or few wavelength DIAL is that for sufficiently closely spaced wavelengths, the target reflectance and LIDAR system response should be approximately constant, and therefore ratioing of signal returns should remove the noise associated with differing background reflectivity as a function of wavelength. This would not be the

case for a MiniFAL system where it is necessary to rapidly tune across much of the CO₂ laser band (9.2-10.7 μm) for the detection of single or multiple chemicals and in the presence of interfering species. The significant wavelength dependent albedo of the background stack emission greatly complicates the problem. Because of the issues with prior algorithmic approaches stated above, a new multiwavelength detection and CL estimation algorithm for MiniFAL applications was formulated. This new approach uses well established techniques of multivariate statistical inference theory, in particular the likelihood ratio test methodology is used to produce optimal estimators for CL and its uncertainty as well as detection algorithms for the presence of vapor. In addition to addressing the problem of broad wavelength coverage, the new method also optimizes noise reduction techniques. Three sets of assumptions about the nature of the spectral background were analyzed, namely (1) a spectrally uniform background, (2) a background with a priori known relative spectral response, and (3) the case of arbitrary backgrounds for which a sample of data collected prior to the introduction of vapor is available. The initial algorithm formulations derived for these three cases were successfully tested with synthetic data and in some cases with actual field data obtained with a FAL. The results show the superiority of the new approach over the conventional two-wavelength ratio analysis. Further work is required to complete the algorithms, include noise smoothing functions, fully code the mathematics, test them (and modify them if necessary) in the critical case of range-resolved detection, and to automate the data analysis process.

In the absence of a fully developed algorithm to provide guidance and to make the process of wavelength selection tractable at this stage of scenario development, a selected list of chemicals was analyzed and only the wavelengths corresponding to the peaks and valleys of the absorption spectra were designated. Emission at the absorption peaks was considered to be an absolute requirement of the sensor. In that respect, it was found that some chemicals of interest did not have any absorption features in the typical wavelength range of the CO₂ laser. Of course, this was known from work in the FAL program. As a result of the FAL related problem, efforts were initiated under a related program at Hughes to investigate techniques for shifting the wavelengths of the CO₂ laser. This investigation showed that wavelength shifting by a combination of SHG (second harmonic generation) and OPO (optical parametric oscillation) could provide access to all chemicals known to be of interest to the Army. Preliminary work on SHG and OPO has been reported in the literature and it is believed that these techniques could be further developed with relatively low risk.

2. INTRODUCTION

Differential absorption LIDAR (DIAL) based on CO₂ laser transmitters is a well established technology for the detection of chemicals in the atmosphere judging by its deployment on a number of mobile platforms. These sensors typically have been designed to address several operational scenarios at once and by their universal nature are relatively large and complex. The development of compact sensors keyed to a restricted set of specific missions has not received much attention. Such development has been hampered to a great extent by the lack of compact laser sensors with good performance at moderate repetition rates, reliable and rapid wavelength shift capability, and long lifetimes.

Recent work at Hughes in the area of high power, compact, frequency stable waveguide lasers and in the area of compact, long life TEA lasers offers the possibility of development of compact chemical sensors. The cw waveguide laser naturally applies to the case of heterodyne detection and the TEA laser applies to the case of direct detection. Both cases are analyzed in this report and it is shown that heterodyne detection provides greater range capability than direct detection. Although use of coherent, cw waveguide lasers in heterodyne systems can provide greater range, achieving wavelength agility while maintaining coherence is a problem that remains to be solved with such systems. Furthermore, the issue of speckle averaging for a coherent system in the case of CL (concentration-path length product) measurements by reflection from topographic features has not been addressed. Alternatively, it has been shown that the range for direct detection systems can be greatly extended to the order of 5 km in the special case of detection of stack gas emissions. The apparent large backscatter coefficient provided by entrained aerosols and particulates in common stack emissions provides for this enhanced range capability. Finally, practical considerations having to do with system complexity, size, and weight favor the TEA laser. In that respect, the prior work at Hughes on compact TEA lasers shows that a device suitable for a compact sensor can be developed with low risk.

This report contains the work accomplished in a program with the objective of providing a feasibility study for MiniFAL sensor development. The study includes (1) analysis and tradeoffs of direct and coherent detection systems for a variety of sensor parameters and mission scenarios, (2) a conceptual design of the most promising system resulting from the sensor analysis, (3) an outline of the mathematics for a new algorithm for the MiniFAL mission and its application to field data, and (4) a selection of laser emission wavelengths suitable for the detection of selected chemicals.

The body of the report begins in Section 3 with details of performance analysis for a large matrix of system designs. The analysis treats multiple parameters related to the laser pulse energy, laser power, atmospheric transmission factor, atmospheric backscatter coefficient, and telescope receive aperture. The special case of data analysis related to stack gas emissions is handled in Section 3.4. The MiniFAL laser design is presented in Section 4. The prior work upon which the design is based is reviewed first, followed in subsequent subsections with details of the conceptual design, details of the important weight analysis, and the areas where further work is required to support the MiniFAL development. The new algorithm that was developed in the program to support the MiniFAL mission is reviewed in Section 5. This includes separate

subsections devoted to the three assumptions about the target background. Section 6 contains the analysis of wavelengths appropriate to detection of a selected set of chemicals. Section 7 contains the general conclusions to be drawn from the program and recommendations for further work.

3. PERFORMANCE ANALYSIS

This section contains the results of analysis for both direct and heterodyne detection chemical sensors. An extensive matrix of scenarios was analyzed that fully encompassed the range of systems and conditions applicable to the development of a man-portable system. As a result, several promising systems were identified for further study. In the case of scenarios where the laser beam was reflected off topographic features, the results were not surprising. Sensors using either direct or coherent detection performed reasonably well. In the case of range-resolved targets, where backscatter from the atmosphere was important, it was also not surprising that range performance was greatly reduced from the topographic reflection case, with the direct detection sensor suffering much more than the coherent system. In that respect, the direct detection systems had ranges much less than 1 km and the coherent systems had ranges on the order of 1-2 km for a variety of receive telescope apertures. Importantly, however, it was found that when the radar model was applied to an extrapolation from actual data with the direct detection system, the predicted range-resolved capability was greatly extended to 5 km. Results in the literature for range-resolved, direct detection of stack emissions supports this contention. The prevailing notion is that the backscatter coefficient for stack emissions is about a factor of 10^4 higher than the presumed atmospheric backscatter coefficient. Therefore, in the absence of conclusive field data, it appears that both the direct and coherent detection systems can be applied successfully to the detection of stack gas emissions. There are other operational and systems issues that would favor one or the other detection approach, but that discussion is outside the scope of this report.

3.1. ANALYSIS MATRIX

The performance analysis matrix is shown in Table 3-1. It addresses systems using both direct detection and coherent detection for the scenarios of DIAL measurement of CL using returns from naturally occurring topographic features, range-resolved measurements of chemical clouds where atmospheric backscatter is used, and the cooperative case where returns are obtained from retroreflectors. The objective was to design a sensor with a MDCL of 100 mg/m² using an absorption coefficient of 10^{-3} m²/mg, typical of the simulant triethylphosphate (TEP) at the strong 9P24 emission line of the CO₂ laser. Although it was not necessary to specify the laser hardware, nonetheless the direct detection system was envisioned as utilizing a moderate repetition rate TEA CO₂ laser producing a train of gain-switched pulses. In this case, no laser frequency control was assumed and the laser was assumed to run freely over its multiple longitudinal and transverse modes. The coherent system was assumed to be a typical, frequency stabilized waveguide CO₂ laser in a homodyne configuration.

For all cases shown in Table 3-1, receiver apertures of 4, 6, and 10 in were used with atmospheric attenuation of 1.6 and 2.3 dB/km. In the case of direct detection, laser energies of 60 mJ and 120 mJ were analyzed, while for the coherent detection systems, cw laser powers of 2.5 and 12 W were used. For reflection from topographic features, a total Lambertian reflectivity of

6% was assumed; and for the range-resolved systems, atmospheric backscatter coefficients of $4 \times 10^{-7} / \text{m} / \text{sr}$, $10^{-7} / \text{m} / \text{sr}$, and $10^{-8} / \text{m} / \text{sr}$ were used.

Table 3-1. Performance analysis matrix.

Parameter	Value
Range Scenario	1-5, 5-8, 8-10 km Topographic return Range resolved
Detection	Retroreflector
Laser energy/power	Direct, Coherent Direct: 60, 120 mJ Coherent: 2, 10 W
Telescope diameter	4 in, 6 in, 10 in
Vapor	Chemical with gray scatterers
Topo reflectivity	6%, Lambertian
Backscatter coeff.	4×10^{-7} , 10^{-7} , $10^{-8} / \text{m} / \text{sr}$
Chem absorption coeff	$10^{-3} \text{ m}^2 / \text{mg}$ (TEP at 9P24)
CL	100 mg/m^2
Atmos attenuation	1.6, 2.3 dB/km
Acquisition time	10 s
Signal/Noise	5
Transmitted lines	<10

3.2. LASER RADAR MODEL

The Hughes laser radar code was used to analyze sensor performance for a comprehensive matrix of scenarios. The code has been proven on a number of programs at Hughes involving both direct detection and heterodyne detection systems. This includes production programs for the M1 tank rangefinder, EN6 Doppler velocimeter and development programs such as the RAS and FAL chemical sensors and SPD and ATLAS imaging radars.

The laser radar model incorporates a number of interdependent parameters including details of the laser, propagation path, target, transceiver optics and electronics, and the statistics of detection. A block diagram of the model is shown in Figure 3-1.

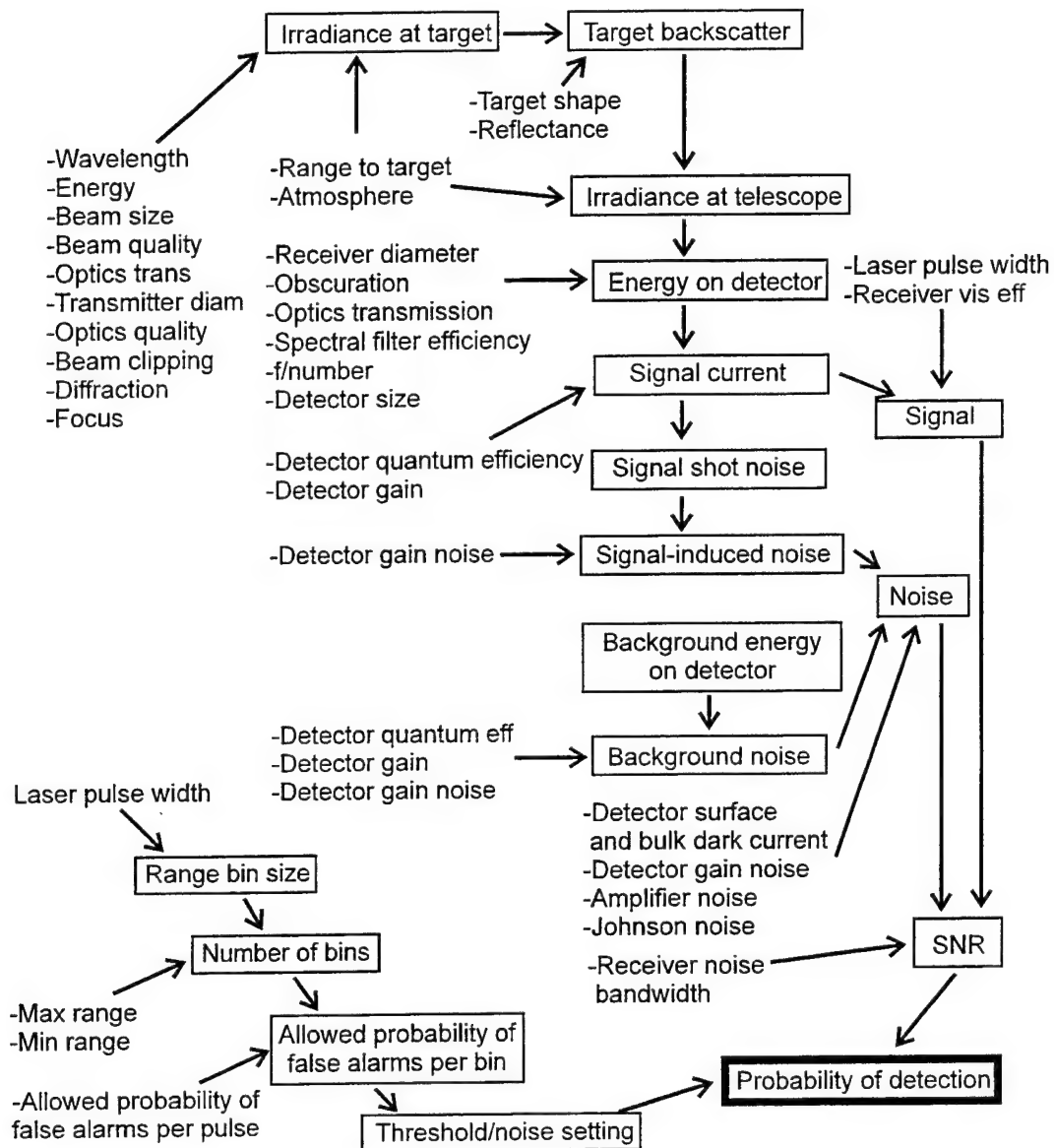


Figure 3-1. Laser radar model block diagram.

The parameters used in the model for the direct detection and coherent detection cases are shown in Tables 3-2 and 3-3, respectively.

Table 3-2. Direct detection sensor parameters.

Characteristic	Value
Pulsewidth	100 ns
Transmit optics efficiency	0.73
Receive optics efficiency	0.78
Receive area obscuration efficiency	0.85
Detector D*	$6 \times 10^{10} \text{ cmHz}^{1/2}/\text{W}$
System f/#	1.3
Detector dia	200 μm
Number of longitudinal modes	4
Random variation/pulse	0.075
Systematic variation	0.015
Receiver field of view	1 mrad
Signal bandwidth	3 MHz
Receiver bandwidth	3 MHz
Pulse visibility efficiency	0.8
Range resolution	15 m
Detector quantum efficiency	0.75
Preamp noise	$0.06 \times 10^{-9} \text{ W}$
Detector NEP, including preamp	$0.51 \times 10^{-9} \text{ W}$
System NEP at aperture	$0.97 \times 10^{-9} \text{ W}$

Table 3-3. Coherent detection sensor parameters.

Characteristic	Value
Number of shots per line	32,000
Chirp rep rate	200 KHz
Chirp duration	4 μs
Chirp duty cycle efficiency	0.8
Energy per chirp	10 or 48 μJ
Chirp bandwidth	5 MHz
BT product	20
Range resolution	45 m
Transmit beam divergence	40 μrad
Transmit optical efficiency	0.73
Receive optical efficiency	0.78
Field loss efficiency	0.8
Focus range	7 km
Target polarization efficiency	0.5
Heterodyne target mixing efficiency	0.37
Doppler velocity acceptance	10 m/s
Detector quantum efficiency	0.7
Signal processing efficiency	0.75
Receiver bandwidth	3 MHz
Detector NEE	$2.7 \times 10^{-20} \text{ W/Hz}$
Detector NEP	$8 \times 10^{-14} \text{ W}$

3.3. ANALYSIS RESULTS

This section contains the results of analysis using the radar model with the standard atmospheric backscatter coefficients ranging from 10^{-8} to $4 \times 10^{-7}/\text{m/sr}$. The results are plotted in Figures 3-2 to 3-9. The special case of the presumed much larger backscatter coefficient pertaining to stack emissions is discussed in Section 3.4.

For the case of reflection from naturally occurring topographic features, the results are shown in Figure 3-2 for direct detection and in Figure 3-3 for coherent detection. The results show reasonably good range performance with the coherent system achieving about 1.5 times the range of the direct detection system.

The direct detection system results are shown in Figures 3-4 and 3-5 for the case of range-resolved targets and for the two values of atmospheric attenuation. It is seen that at least an 8 in diameter receive telescope and the maximum values of laser output energy and backscatter coefficient are required to reach ranges on the order of 1 km. Increased atmospheric attenuation has a modest effect on range.

Results for the case of range-resolved targets with coherent detection systems are shown in Figures 3-6 and 3-7. It is found that for aperture and atmospheric attenuation values comparable to the direct detection system, the coherent system can reach to ranges of 3 km at the highest power and to 2 km at the lowest power. The latter range is a factor of two greater than that achieved with the higher power direct detection system.

The DIAL scenario with a retroreflector shows very good range capability as indicated in Figures 3-8 and 3-9 for a direct and coherent detection system, respectively. Ranges are somewhat comparable for the two systems and increasing atmospheric attenuation in the two cases amounts to about a 20% reduction in range.

Finally, the results are summarized in Table 3-4.

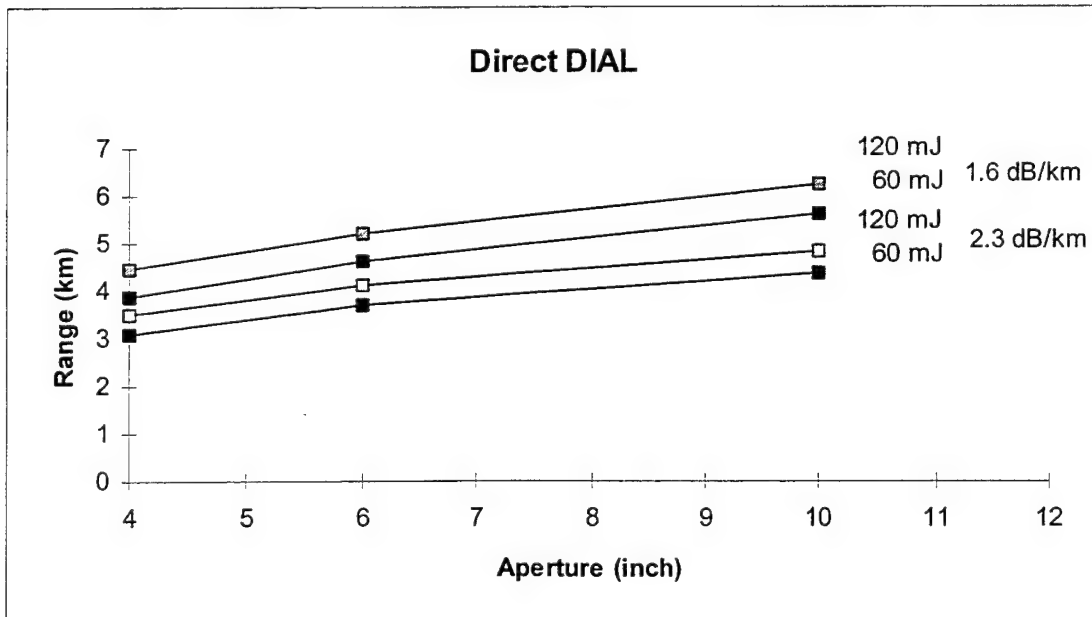


Figure 3-2. Range capability of direct detection topographic DIAL systems.

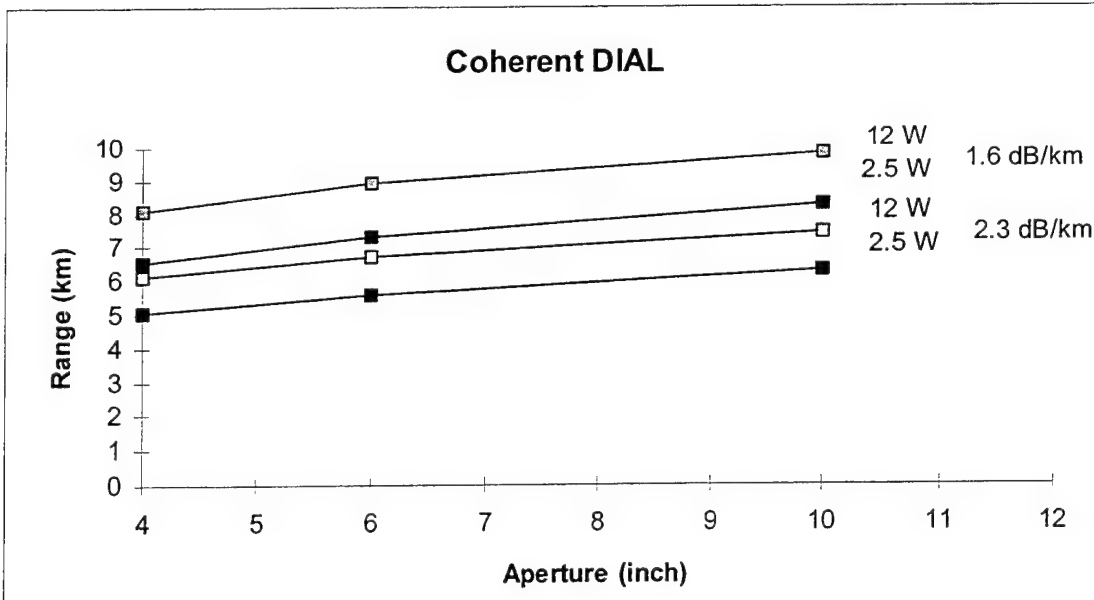


Figure 3-3. Range capability of coherent detection topographic DIAL systems.

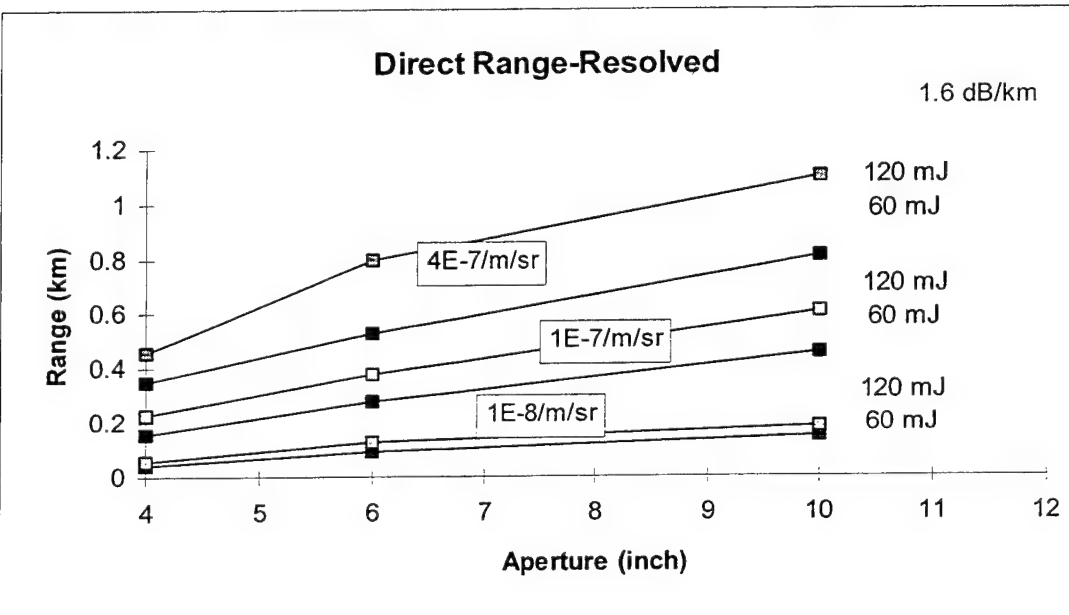


Figure 3-4. Range capability of direct detection range-resolved system for 1.6 dB/km.

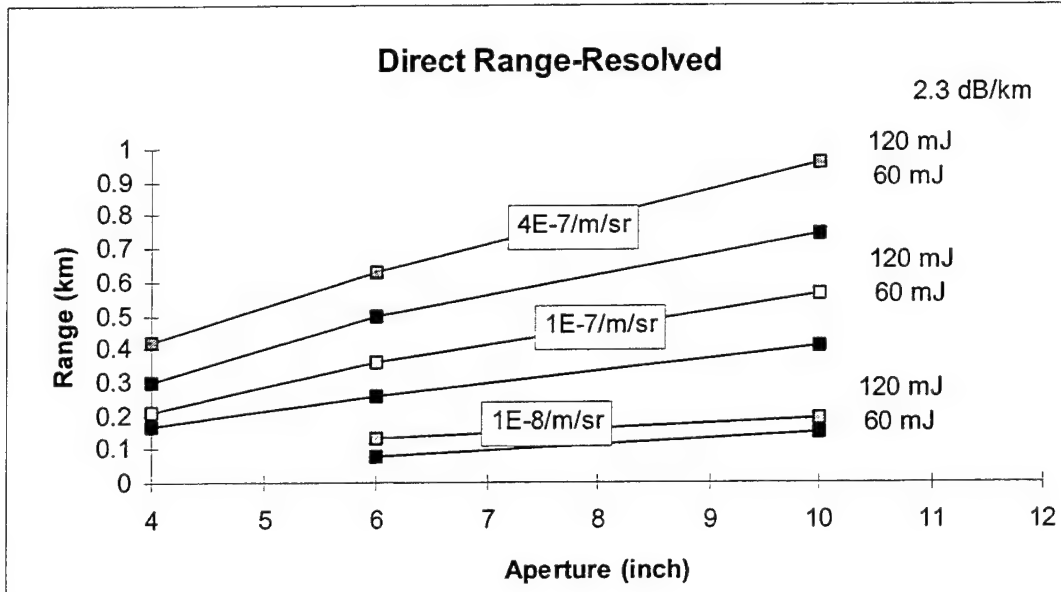


Figure 3-5. Range capability of direct range-resolved system for 2.3 dB/km.

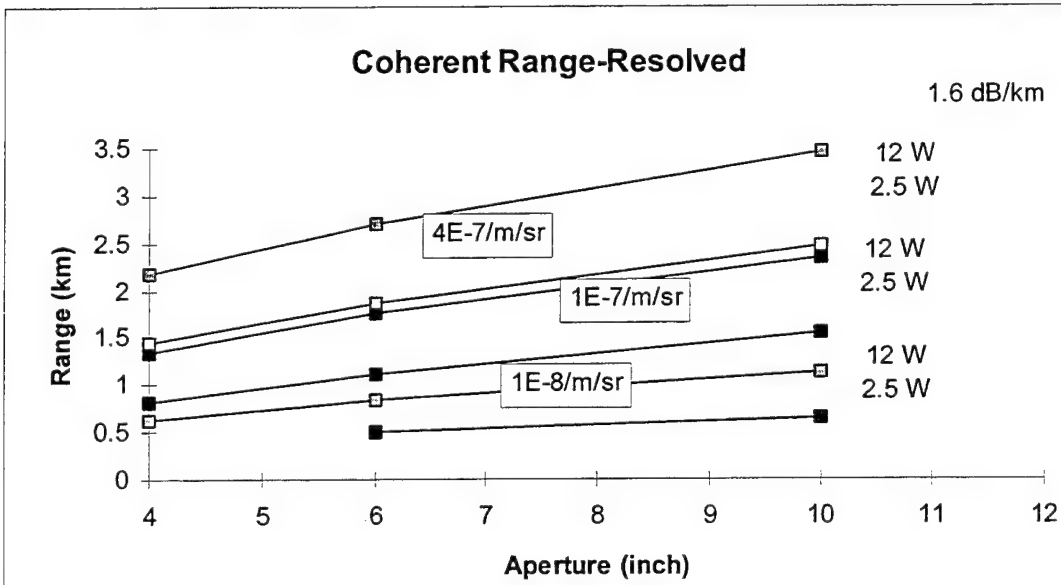


Figure 3-6. Range capability of coherent range-resolved system for 1.6 dB/km.

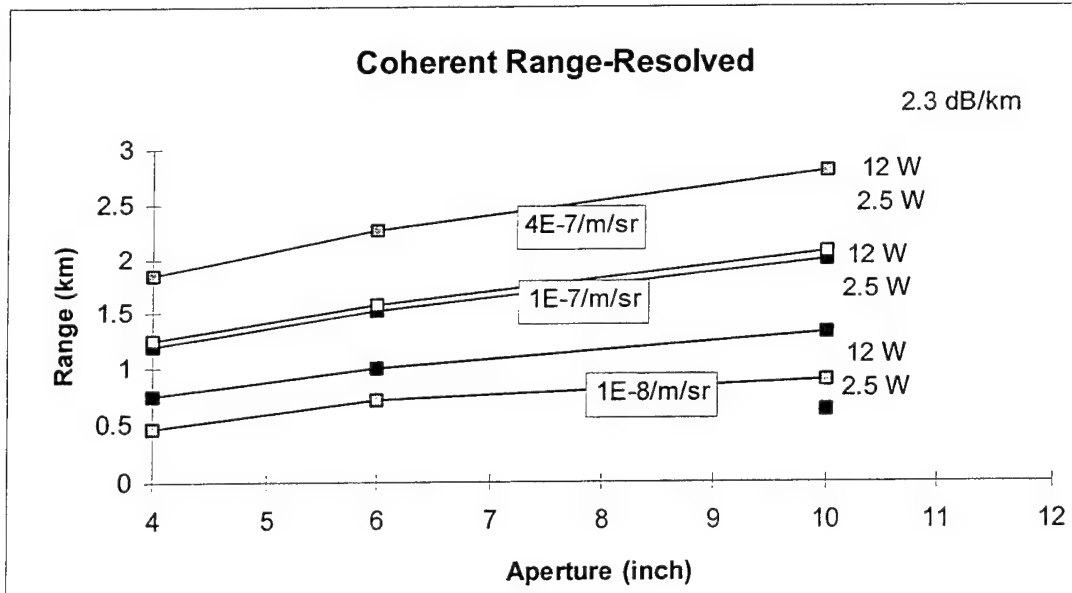


Figure 3-7. Range capability of coherent range-resolved 2.3 dB/km system.

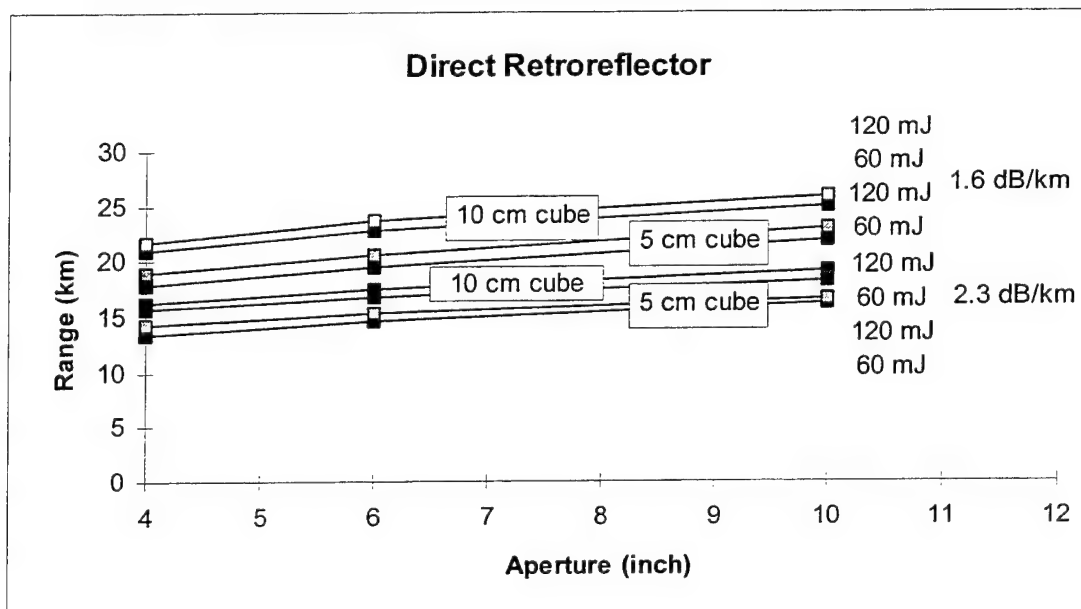


Figure 3-8. Range capability of direct DIAL system with retro.

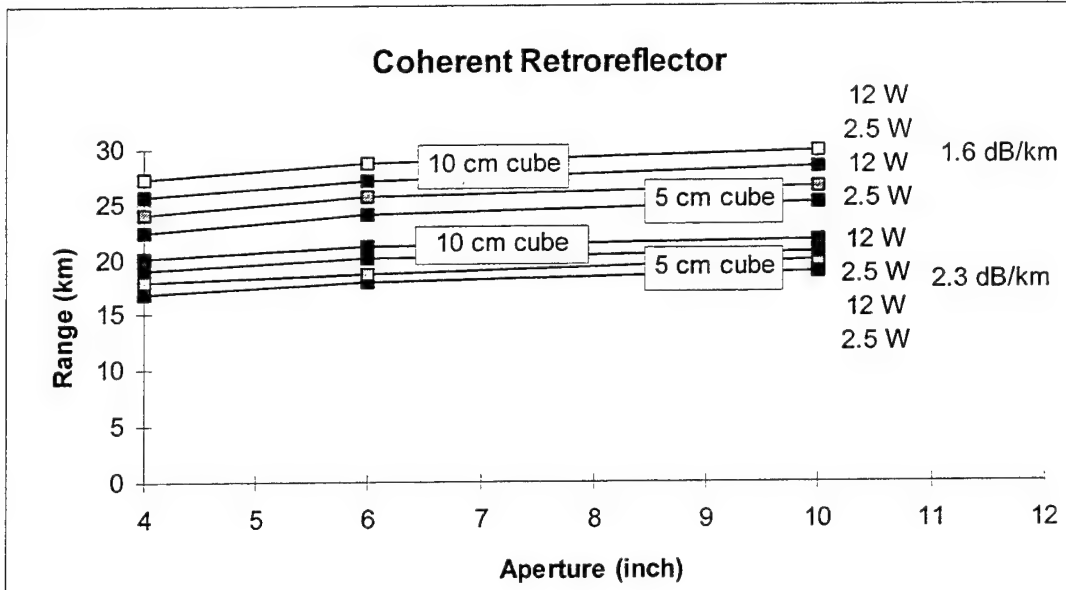


Figure 3-9. Range capability of coherent DIAL system with retro.

Table 3-4. Performance analysis results.

Detection Method	Atmos (dB/km)	Range (km)			Range-Resolved Tele dia (in)		
		4	6	10	4	6	10
Direct	1.6	3-4.5	4.5-5.5	5.6-6.2	0.18-0.2	0.25-0.35	0.4-0.5
	2.3	3-3.5	3.5-4	4-4.5	0.18-0.2	0.25-0.35	0.4-0.55
Coherent	1.6	6.5-8	7.2-8.8	7.5-9.3	0.8-1.4	1.1-1.7	1.3-2.2
	2.3	5-6.2	5.5-6.5	6-7	0.75-1.3	1-1.5	1.2-1.75
Retro-Direct	1.6	22-24	23.5-25.5	24.5-27			
	2.3	17-18	17.5-18.5	17.5-18.5			
Retro-Coh	1.6	17-18	17.5-18.5	17.5-18.5			
	2.3	22-24	23.5-26	25-27			

Notes: Lower value of range for laser output of 60 mJ/20 Hz (direct) or 2 W (coherent) and higher values for laser output of 120 mJ/100 Hz (direct) or 10 W (coherent)
 Range-resolved results for 10^{-7} /m/sr scattering coefficient
 Retroreflection results for 5 cm dia corner cube

3.4. RANGE-RESOLVED CONSIDERATIONS

As shown in the analysis above, direct detection systems have limited range where the naturally occurring atmospheric aerosols are used as backscatterers. It was shown that the range with a transmitter emitting 120 mJ would be only several hundred meters with a 4 in diam telescope and about 500 m with a 10 in diameter telescope. Therefore, under the usual assumptions about the operational scenario, direct detection systems are very limited. However, this range limitation is critically dependent upon the details of the target and it may not apply in selected cases. One important application where this has been shown to be true is in stack gas

emission detection. Published data show that a direct detection system of the type under consideration here can perform very well out to ranges on the order of 2 km for chemical concentrations on the order of parts per billion and that the range can be extended to 5 km for concentrations of parts per million.¹ The reason for this greatly extended range is the presence of water aerosols and particulates in typical stack emissions which increases the effective backscatter coefficient about a factor of 10^4 . The use of direct detection systems for range-resolved detection has also been verified in the use of broadband spectral scans for detection of multiple chemical species in the presence of interferences, a condition typical of a MiniFAL mission.

Evidence for the high backscatter in clouds was also seen in typical data taken with the FAL system at Hughes. Typical data is shown in Figure 3-10 for a return from a rain cloud using a laser output energy of 100 mJ and a 10 in diameter telescope. The trace of Figure 3-10 shows a transmit pulse with a width of 150 ns. The receive pulse shows the usual broadened return from near-range aerosols out to about 500 m (3.3 μ s). Note (as discussed in Section 4) the peak in this return at a range of 120 m is due simply to the transmit pulse spreading beyond the telescope secondary. This broadened, near-range return is the subject of the analysis above.

The interesting aspect of the data is the strong return from the rain cloud located at a range of about 1.5 km. The cloud return is broadened, compared to the transmit pulse, suggesting that the extended cloud target was sufficiently penetrated. The strong return is likely due to specular reflection from water droplets or aerosols. In any case, the atmospheric backscatter coefficient was derived from the near-range return and the laser radar model was applied using a coefficient extrapolated to the apparent value pertaining to the cloud. The analytical results showed that for chemicals such as TEP and CL values of 100 mg/cm^2 , the range-resolved detectability could indeed be extended to 5 km as shown by others in the field.

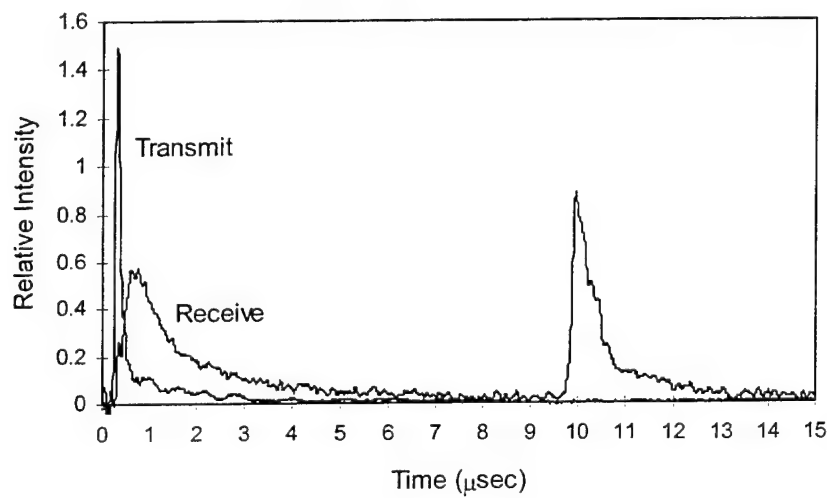


Figure 3-10. FAL direct detection with range-resolved cloud.

4. LASER AND SENSOR DESIGN

The MiniFAL laser and sensor designs are based on hardware developed under a Hughes IR&D program and on equipment developed under the FAL program with the U.S. Army CBDC.² With respect to the MiniFAL laser, its design is derived from a device developed at Hughes in 1988 to validate an initial design of a fully integrated, high repetition rate laser called the Modular TEA Laser. This program was highly successful and resulted in a transmitter that was subsequently integrated with a long range rangefinder and tested in the field in several campaigns. The Modular TEA was the first laser at Hughes to demonstrate a number of critical components necessary for sustained high repetition rate operation in a compact device, including a sealed vessel with internal catalyst, high repetition rate operation of a sparkgap high voltage switch, and a high speed tangential fan.

The FAL program which followed the Modular TEA development contributed a great deal to the laser critical component data base, primarily in the areas of sealed operation with a catalyst, wavelength shifting, and long life optical resonators. The FAL laser underwent successful environmental testing and has been operated under a variety of conditions in the field without failure. In addition to laser development, a primary goal of the FAL program was demonstration of a brassboard, fieldable chemical sensor. This development resulted in a robust data collector that participated successfully in three field campaigns over a four year period resulting in complete data sets for a number of scenarios, including aerosol clouds, vapor chambers, manmade and natural hard targets, and chemicals dispersed on various media. In summary, the prior work on laser and sensor development has a direct bearing on the MiniFAL laser and sensor designs and greatly reduces the risk in their development. The various specific contributions are as follows:

Prior Program	Contribution to MiniFAL
Modular TEA laser	<ul style="list-style-type: none">-Compact laser design-Component validation
FAL laser	<ul style="list-style-type: none">-Sealed vessel with catalyst-Long life bearings-Long life resonator-Vessel processing technique-Optical layout
FAL sensor	<ul style="list-style-type: none">-Data acquisition electronics-Post-processing software-Data analysis

Presented in this section are brief descriptions of the Modular TEA laser and the FAL laser and sensor since these devices are essential to the MiniFAL design. Presentation of the MiniFAL design follows the description of this prior work.

4.1. PRIOR WORK

4.1.1. Modular TEA laser

The Modular TEA laser is a transversely excited type wherein the high speed gas flow direction, optical axis, and discharge electric field are orthogonal. The laser discharge is defined by two opposing electrodes of small aspect ratio, width to length; and the gas is excited by a fast, high current discharge. For operation at high pulse repetition rates up to 100 Hz, it is necessary after each discharge to remove the gas from the inter-electrode region prior to the next pulse in order to avoid arcing. This is accomplished by a tangential fan which circulates the gas at high speed through the electrode region and also moves it through a parallel heat exchanger and catalyst module. The internal catalyst module is required to reconstitute the CO₂ decomposed in the discharge process. The optical mode cross-section is defined by the discharge height and width which in the case of the Modular TEA laser is a 1 cm square. The output temporal profile is a typical gain-switched spike of about 150 ns duration, followed by a 1 μ s long, low intensity tail.

A photograph of the integrated Modular TEA laser is shown in Figure 4-1. Note the 6 in. long scale. From top to bottom in the picture, the laser head is constructed in four sections, including (1) the high voltage section composed of the high voltage capacitors, sparkgap high voltage switch, and sparkgap high voltage trigger generator; (2) the gas discharge section composed of the electrodes and preionization discharge; (3) the catalyst section composed of the catalyst module and thermocouple temperature diagnostics; and (4) the tangential fan housing. The high voltage power supply that charges the energy storage capacitor bank is shown to the left of the laser head.

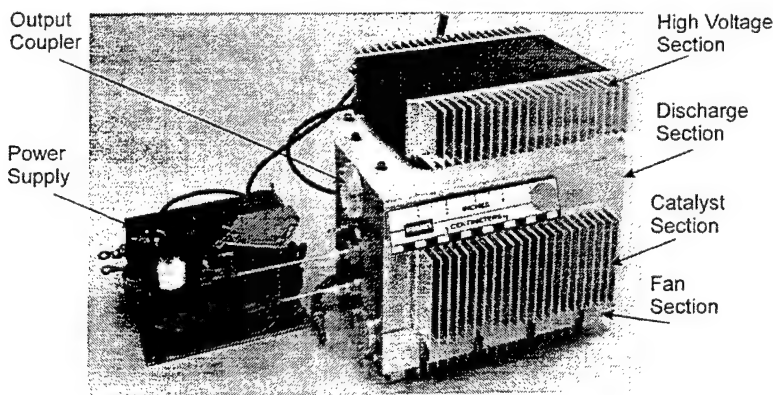


Figure 4-1. Modular TEA laser.

The specifications of the Modular TEA laser are shown in Table 4-1. Note that the wavelength scanner was not used on this device; therefore, the total number of wavelengths available was not determined. Based on tests with the FAL system, it is anticipated that approximately 50 mJ would be available on weak lines such as 9P44 and that about 55 lines over the CO₂ spectrum would be accessible. Furthermore, the weight of the device was not measured because it was not important to either the IR&D or rangefinder programs and because of design modifications discussed below, it would not be relevant to the MiniFAL design.

Table 4-1. Modular TEA laser specifications.

Pressure vessel	Sealed with catalyst
Output energy	120 mJ, strong lines
Modes	Multi-transverse
Wavelengths	~55
Repetition rate	100 Hz, 50% duty cycle, 50 Hz continuous
Isotopes	$^{12}\text{CO}_2$ or $^{13}\text{CO}_2$

The overall laser head length of approximately 9 in. is determined by the electrode length and the spacing required at each end to prevent discharge arcing to the grounded case. The width of the laser head is determined by the combined electrode width, the high voltage standoff distance and the minimum radius necessary to achieve fast tangential gas flow. The height of the Modular TEA laser was determined by the need in the prototype configuration to diagnose the catalyst module temperature and gas glow velocity; therefore, it was made much larger than would be required in a final device. It is anticipated that the catalyst module could be made integral with the tangential fan assembly (as it is in the FAL laser) in which case the overall height of the laser could be reduced by 50%.

A conventional capacitive discharge circuit is used to pump energy into the laser discharge as shown in Figure 4-2. The elements of the circuit include a command charge power supply that converts 28 Vdc to 25 kV, ceramic energy storage capacitors, a sparkgap high voltage switch, and the discharge module. It was necessary in the IR&D program to identify and verify operation of these components for long life operation.

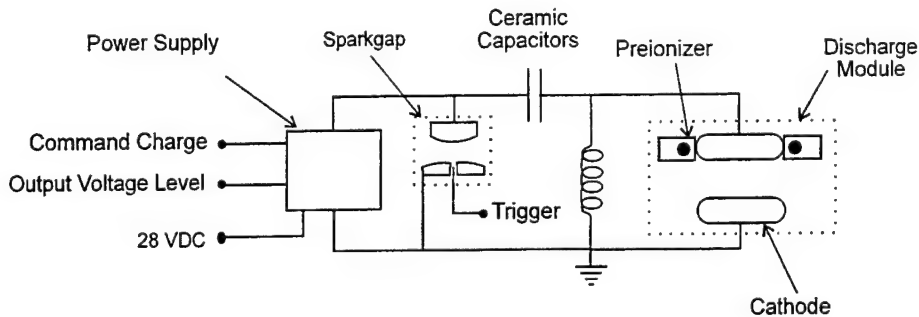


Figure 4-2. High voltage section.

The optical resonator for the Modular TEA laser shown in Figure 4-2 was composed simply of a total reflector with 10 m radius of curvature and a flat output coupler with 86% reflectivity at 10 μm . Both optics were attached to the discharge module which held them in reasonable alignment. This resonator was modified for application to a frequency-stable rangefinder which included a stiff aluminum, surrounding, independent optical bench to which was attached the output coupler on one end and a piezoelectrically driven total reflector on the other end. This arrangement was successful in maintaining a cavity shot-to-shot frequency stability of 5 MHz. For operation with an agile grating as envisioned with the MiniFAL design, it will not be necessary to stabilize the cavity, but it will be required to add a low thermal coefficient of expansion optical bench around the discharge module to achieve the required alignment stability over temperature excursions. This approach was proven in the FAL design.

The Modular TEA laser was very successful in several field tests at White Mountain, California at an altitude of 10,000 ft. In those tests it was operated with the $^{13}\text{CO}_2$ isotope for emission at 11 μm , proving the stability of the catalyst for both standard and isotopic gas mixtures. The laser is still operating as of this writing.

4.1.2. Frequency Agile Laser

The FAL laser is derived from the basic work carried out on the Modular TEA prototype but with the added requirements for a factor of two increase in output energy, a factor of two increase in repetition rate, wavelength agility, and the capability to withstand environmental stresses. A picture of the device is shown in Figure 4-3. A 6 in. long ruler is shown at the foot of the along the edge of the base plate. The ribbed structure at the top is the section of the pressure vessel housing the air-cooled heat exchanger, catalyst module, and internal fan. Surrounding this section of the vessel is a rectangular graphite-epoxy composite optical bench to which are attached the wavelength shifter and the output coupler assembly. These components are optically coupled through Brewster windows attached to the vessel. Beneath the optical bench and pressure vessel are located the fire control electronics and high voltage power supply. The laser is sealed and completely self contained as shown and requires only a source of 28 Vdc and RS-232 link to the computer to operate.

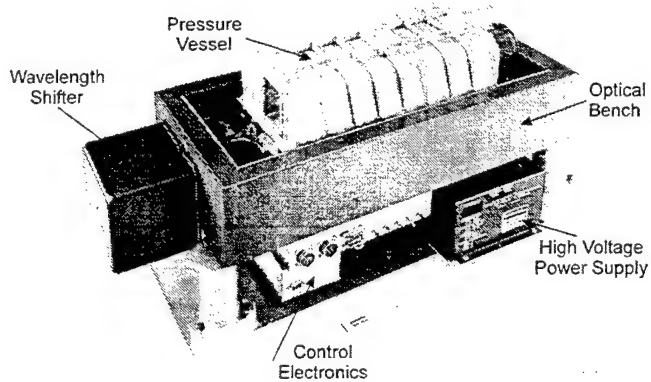


Figure 4-3. Frequency Agile Laser.

The FAL optical resonator is a unique design required to eliminate optical damage on the output coupler as discussed below. The resonator, shown schematically in Figure 4-4, is composed of the wavelength shifter on one end and an intracavity beam expander on the other. The 3x expansion reduces flux on the coupler and allows for a high output coupler reflectivity of 85% which is essential to maintain good power extraction on both strong and weak lines. The MiniFAL will also make use of an intracavity expander, but it will serve the dual purpose of beam expansion for sensor divergence control.

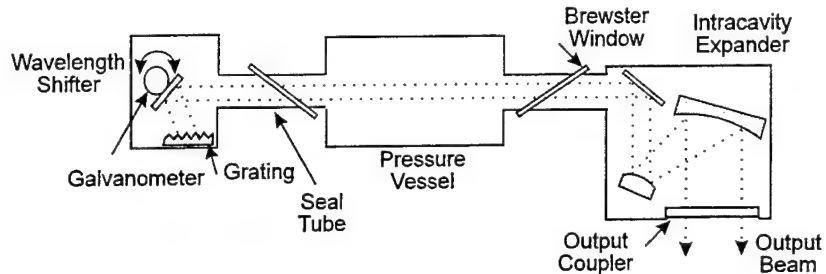


Figure 4-4. FAL resonator schematic.

The objective of the FAL program was to meet a number of physical constraints and functional requirements. These program requirements and the achieved FAL values are shown in Table 4-2.

Table 4-2. FAL specifications.

Characteristic	Requirement	FAL	Comments
Lifetime	Design for 10^8 shots Test to 5×10^7 shots	Yes	Optics failure in lifetest-eliminated in redesign, no other failures noted
Output Energy	>100 mJ, all lines	Yes	≥ 115 mJ at 40°C ≥ 140 mJ at 25°C
Pulse length	70% energy in 250 ns, Tail=60 dB down at 1 μsec	70% energy in 250 ns, Tail=20 dB down at 1 μsec	3 crystal chopper 20 dB limit of diagnostic resolution
Wavelength Tuning	1-16 lines at 200 Hz rate, 40 % duty cycle	Yes	1-20 lines possible
	55 lines: 9P10-9P44, 9R10-9R30, 10P8-10P32, 10R8-10R32	>65 lines	All bands range J (6-38), Galvo span limits 9R and 10P max
Transverse Modes	>3 modes	10	Inferred from divergence
	<15% spatial energy distribution variation in far field	Yes	Inferred from infrared camera measurements
Temp Range	0°C to 40°C	Yes	Operating
Vibration	± 2 G, 5-500 Hz, 3 axes	Yes	Non operating
Shock	3 ± 0.3 G, 11 ± 1.1 ms half sine, 3 axes	Yes	Non operating
Size	<2 cu ft	3 cu ft	Height increase for modified capacitors
Weight	<50 lb	100 lb	Design mods
Sealing	Hard seals	Yes	Original design all hard seals, NaCl window not hard sealed
Shelf Life	≥ 1 year	Unknown	Tested to 6 mos, no limiting effects known

The FAL achieved all functional requirements and some with margin. The output energy on all lines exceeded the requirement. It was also found that the laser could access additional

lines to rotational J values of 4-6 and up to J values of 44 for the four bands. The firing lifetime was achieved in tests with no failure to 53 million shots for the integrated laser and to 80 million shots for several critical components. Optics were found to damage early in the lifetest; however, redesign of these components have shown that damage can be eliminated. Therefore, life limiting mechanisms are not known and it is likely that the 10^8 shot design point is achievable.

The size and weight requirements were not met. This was due to modifications to several components that were not foreseen at the beginning of the program and that were later dictated by the need to meet lifetime or functional requirements and to minimize cost. In that respect, the components of most importance are the high voltage power supply, energy storage capacitors, electronics packaging, and laser alignment and support hardware.

After development of the first FAL, it was extensively tested (1) for qualification with respect to the functional requirements, (2) under various environmental conditions, and (3) for performance over a 50 million shot life test. Qualification testing involved monitoring laser output and condition while operating at full repetition rate and duty cycle for extended periods. This was done to determine overall laser capability. Subsequently, the environmental and lifetime test sequences were performed. The thermal test involved operation at 0 °C, 20 °C, and 40 °C with a four hour dwell time and functional test at each temperature. The vibration test was conducted with a ± 2 G sine wave sweep from 5 to 500 to 5 Hz along each axis and an average power test was performed before and after each sweep. The shock test involved a series of three, 3 G shocks in both directions of each axis with an average power measurement after each event. Following the thermal, vibration, and shock testing a qualification test was performed prior to lifetesting. Finally, life time testing was carried out with the goal of achieving 50 million shots with testing of laser output after every 5 million shots.

The FAL passed all tests successfully with the exception of optical damage found in life testing. The single, fully integrated, sealed laser was taken through qualification testing, environmental testing, and life testing without failure. In life testing it was operated to 53 million shots with testing terminated by the operator not malfunction. After testing with this particular laser, several components were removed to aid in assembly of two more devices. This included the discharge module, high voltage module, and control electronics. These components were subsequently tested to 75 million shots without failure and their ultimate lifetimes are not known.

The first FAL was configured with a conventional optical resonator and ZnSe Brewster windows. The resonator was composed of an 86% reflecting output coupler with a beam cross-section of 1 cm x 1 cm and it was with this resonator design that optical damage was found to be the life limiting problem. However, redesign of the resonator to incorporate a 3X intracavity beam expander and NaCl Brewster windows has eliminated optical damage in abbreviated life tests.

Testing of the intracavity beam expander to 5 million shots has shown no indication of damage and extrapolations suggest that the lifetime of this component could approach the 100 million shot goal. S.A.T. has tested NaCl Brewster windows to 20 million shots without indication of damage under conditions similar to the FAL. In summary, the new FAL optical designs appear to have solved the optical damage problem, although further testing is recommended. Aside from this issue, a failure mechanism has not been identified that would prevent achieving the 100 million shot life goal.

4.1.3. FAL sensor

The sensor was developed primarily as a testbed for demonstrating chemical detection in the field with the high repetition rate FAL transmitter. In that respect, the design was guided by the need for easily modified components that were readily available and presented low schedule and technical risk. The design approach, therefore, did not favor size and weight reduction in relation to functionality and reliability, although efforts were made to produce as compact a system as possible. This approach resulted in a system that was shown to have good stability, low noise, and superior detectivity. The sensor was successfully tested in three separate field trials at Dugway Proving Ground, Utah in 1992, 1993, and 1995.

The sensor was designed to utilize a mixture of components that were both specially designed and commercially available. In order to satisfy the requirements for performing field experiments, several pieces of diagnostics were included in the sensor design that could be eliminated in order to significantly decrease size and weight. These diagnostics included primarily an alignment HeNe laser, joulemeter, and spectrometer. All sensor components were mounted to a single side of an aluminum optical table for ease of alignment and modification for various experiments, and the table was mounted to a gimbal for pointing in azimuth and elevation. The sensor was supported by a 6 ft high equipment rack housing a power distribution panel, controls for a television camera, signal amplifiers and filters, data acquisition electronics, and an IBM-compatible personal computer (PC). The sensor specifications are summarized in Table 4-3. A picture of the fully integrated sensor mounted to the gimbal and with the data acquisition rack is shown in Figure 4-5.

Table 4-3. FAL sensor specifications.

Characteristic	Specification
Telescope	10 in dia Cassegrain, afocal
Effective focal length	10 in
Field of view	4 mrad
Transmit det type	100 μ m PC HgCdTe, 50 MHz
Transmit det D*	1.94×10^8 cmHz $^{1/2}$ /W
Receive det type	1 mm PV HgCdTe, 5 MHz
Receive det D*	4.6×10^{10} cmHz $^{1/2}$ /W
Gimbal AZ/EL	$\pm 90^{\circ}$ - 5° to $+15^{\circ}$
Data acquisition	Digital oscilloscope or PC card
Vertical resolution	12 bit
Sampling rate	30 MHz
Size	40 in. x 46 in. x 28 in., less gimbal
Weight	250 lbs, less gimbal
Input power	208 Vac, 2 A; 110 Vac, 2 A

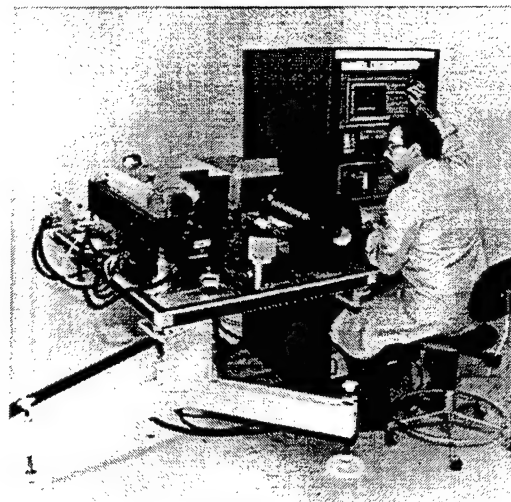


Figure 4-5. FAL sensor.

All optical components were integrated on a single optical bench of dimension 40 in wide, 46 in. long, and 2 in. thick. The bench was made with aluminum face sheets and a lightweight honeycomb core. A schematic of the optical components integrated on the sensor optical table is shown in Figure 4-6. The beam emitted by the laser is turned and reduced (through element 2) to match the aperture of the CdTe crystals. After passing through the tailchopper composed of the CdTe crystals and ZnSe polarization analyzer, the beam passes through a splitter which diverts approximately 2% to a transmit beam monitor. The transmit beam monitor is composed of an

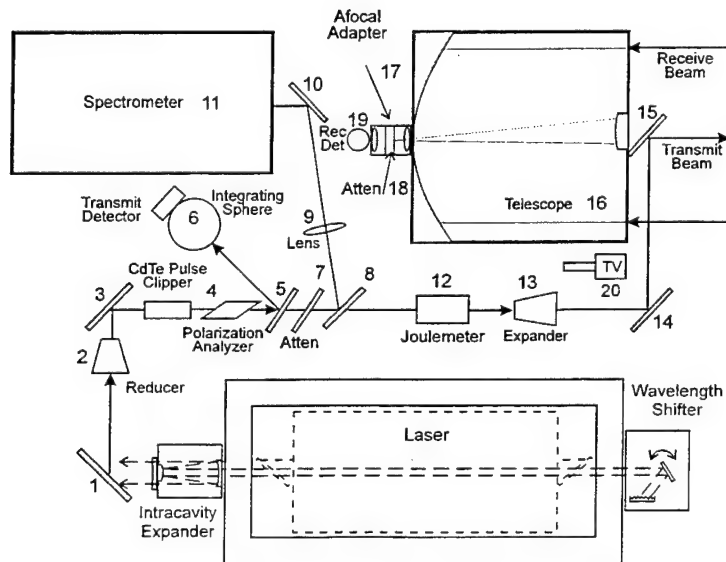


Figure 4-6. FAL sensor optical schematic.

integrating sphere and HgCdTe detector. A holder placed after the transmit beam monitor allows for beam intensity reduction using various ZnSe attenuators (element 7).

In order to observe the emission spectrum, the option exists of inserting a total reflector in the beam path (element 8) on a kinematic mount to divert the entire beam to the spectrum analyzer. In a similar way, observation of total output energy is possible by insertion of a joulemeter on its kinematic mount (element 12). With these elements withdrawn in the normal data gathering mode, the beam is enlarged through the expander (element 13) and is propagated to the scene by the beam directing mirrors (elements 14 and 15).

The beam returned from the scene is collected by the Cassegrain telescope and focused through the primary mirror to an afocal region of 1 in. dia. The afocal section allows for insertion of attenuators or other optical elements without changing the focal spot position with respect to the field lens. The field lens then focuses the incoming radiation onto the receive detector.

Extensive field tests were performed with the FAL sensor. Importantly, it was found in preliminary testing that the standard deviation of the ratio of return to transmit pulse amplitudes approached 1-2% after a 16 pulse average. This figure is less than those typically quoted in the literature for comparable systems. Furthermore, the standard deviation was found to be proportional to $1/N^{1/2}$, as expected. It was also required that an absolute calibration of target reflectivity be performed. This required a complete knowledge of the transmission factors of all optical elements and the detector responsivities as a function of wavelength. Reflectivity tests with a canvas target calibrated independently gave results within 10% of the sensor net transmit-to-receive throughput. In the field, atmospheric water vapor was periodically measured with the sensor and compared to meteorological instruments. The results were within instrumentation accuracy. With respect to the chemical detection data base, complete data sets were obtained with the sensor using manmade and natural solid targets, vapor chambers, aerosols dispersed from ground sources and from aircraft, and with chemicals dispersed on the ground. Finally, single pulse returns were obtained from natural targets as far away as 12 km, suggesting that with pulse averaging, ranges of 20 km could be achieved. Throughout field testing, the sensor participated in 100% of the tests and continues to perform very well. Normal maintenance problems and peripheral problems with the computer and software were noted and corrected.

4.2. MINIFAL DESIGN

The MiniFAL design has two major components, the laser transmitter and the remainder of the sensor system with which it is integrated. In that respect, the laser design is based on the Modular TEA laser and the sensor layout is patterned after the FAL sensor. With this approach, the MiniFAL design is derived from a decade-long line of development of critical components, prototype laser heads, sensor systems, and field experience. The MiniFAL design requires further development of certain components and subsystems, but it is anticipated that the associated risks will be manageable. These development tasks are discussed in Section 4.3.

An artist's rendering of the conceptual MiniFAL design is shown in Figure 4-7 and a schematic view of the sensor is shown in Figure 4-8. Note the overall length dimension of 14 in. Given an overall height of 12 in and a width of 6 in., the total sensor volume is 0.63 ft^3 . As shown

below, weight projections based both on existing components and well defined development of certain other components suggest a total weight of 33 lb. These parameters clearly put the MiniFAL in the category of portability by one person and it is designed to be operated by a single person. In addition, it is intended that the device be pointed at the target either by hand (for near-range objects) or by a mechanical tripod. The sensor is designed to plug into a battery power source with an output voltage of 12 Vdc. A global positioning system (GPS) provides for position recording and display prior to sensor operation. Data of this type and the target signals are stored on a PCMCIA hard drive which is removable allowing for data reduction at another site where it is envisioned extensive computer resources would be available for post-processing. The optical architecture is fundamentally the same as for the FAL sensor with the important exception that the transmit and receive beams are not colinear. The transmit beam detector with integrating sphere receives its input from a beamsplitter in front of the final beam director. The detector electronics, data acquisition electronics, and data storage media are packaged behind the telescope primary mirror. The sensor system also includes a standard off-the-shelf video camera and video display. The laser and sensor specifications are summarized in Table 4-4. Note that the repetition rate of 30 Hz is a nominal design point and that a range of 30-50 Hz is feasible with the present design. It has been shown by Fox, et al that rates at the higher end of the range are desirable ³.

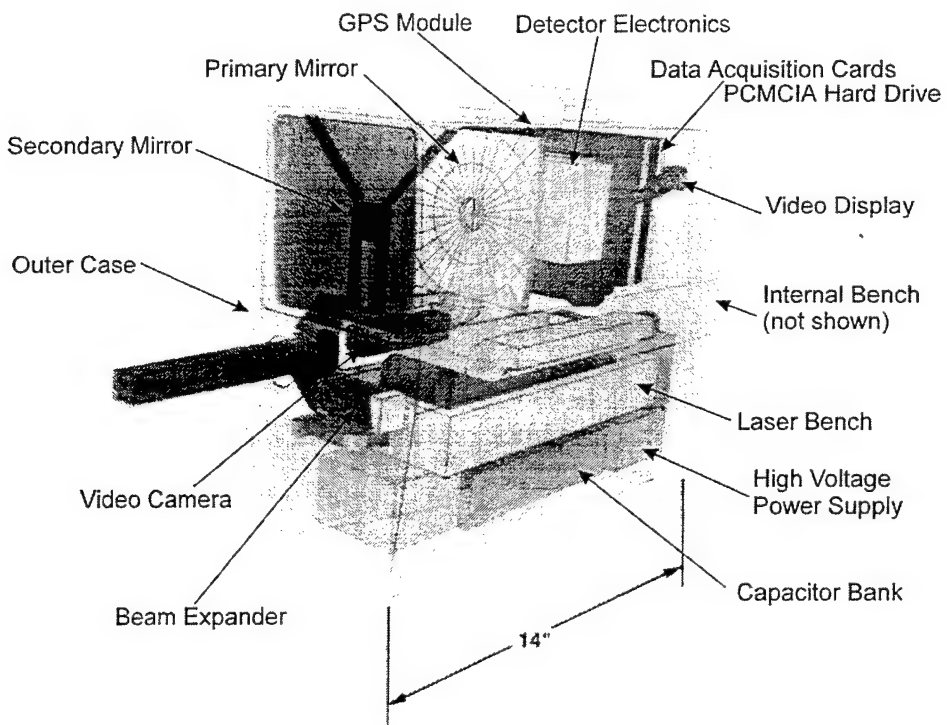


Figure 4-7. MiniFAL conceptual design.

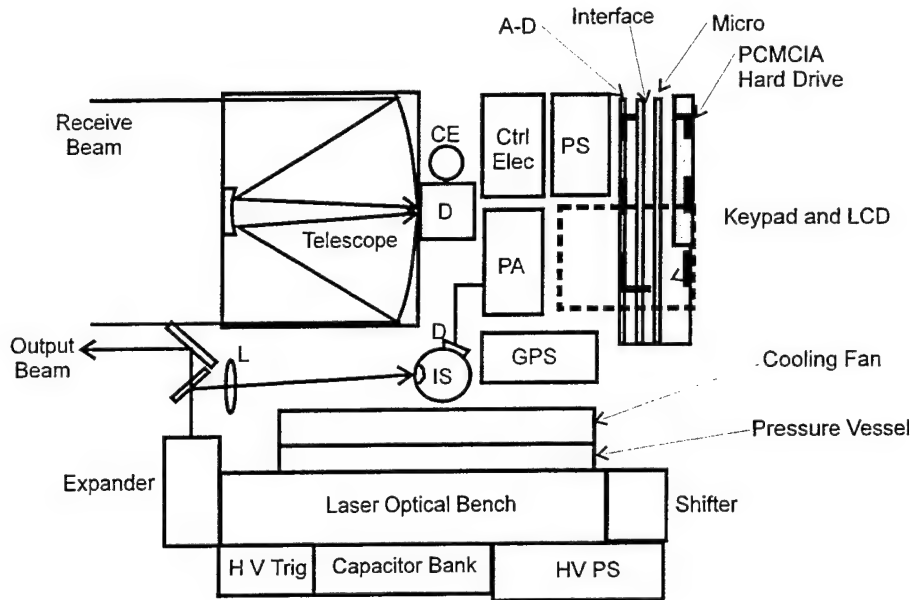


Figure 4-8. MiniFAL component layout.

Table 4-4. MiniFAL specifications.

Laser		Sensor	
Characteristic	Value	Characteristic	Value
Output energy	>50 mJ, all lines	Telescope aperture	5 in x 5 in
Rep rate/shift rate	30 Hz	Telescope type	Cassegrain
Wavelengths	55, 9.3-10.7 μ m	Transmit detector	PC HgCdTe
Patterns	20 lines, any order	Receive detector	PV HgCdTe
Divergence	3 mrad full angle	Receive D*	5×10^{10} cmHz $^{1/2}$ /W
Vessel	Sealed, catalyst	Data acquisition	2 ch, 30 MHz A-D
Cooling	Forced air	Pointing	Tripod/gun sight
Input voltage	12 Vdc	Overall weight	32 lb
Input current	1 A	Overall size	6 in x 12 in x 15 in
Gas pressure	1 atm	Input power	150 W

4.2.1. Laser

The MiniFAL laser is derived from the Modular TEA laser prototype discussed above. However, as shown by a comparison of the prototype in Figure 4-1 and the MiniFAL concept in Figure 4-7, further development is required in several areas. First, the pressure vessel will be greatly reduced in size and weight because of the elimination of the large catalyst diagnostic module in the prototype. It will be constructed of thin-walled aluminum instead of the monolithic, machined block used in the prototype. Finally, as proven in the FAL design, the vessel will be sealed with long life, noncontaminating gaskets and it will make use of a magnetically coupled internal fan assembly with noncontaminating bearings so as to provide for long shelf life.

A composite optical bench surrounding the pressure vessel will be used in a similar fashion to the FAL design. The wavelength shifter attached to the rear of the bench will be a compact, lightened version of the device used on FAL. A program supported by CBDC is underway to develop this shifter. The Intracavity beam expander attached to the front of the bench will serve the dual purpose of eliminating optical damage on the output coupler and it will provide for the final beam expansion that determines the transmit beam divergence. This expander will use the proven off-axis design with total reflecting mirrors. In order to achieve outputs of 50 mJ on weak lines, the output coupler reflectivity will be increased to 90-96%. It should be noted that effective chemical detection with the MiniFAL sensor can probably be achieved using the 9P40 line which has higher gain than the 9P44 line used with the FAL.

4.2.2. Sensor optics

The receiver optical layout makes use of a 5 in x 5 in square Cassegrain telescope that is biaxial with the transmitted laser beam. This is in contrast to the coaxial FAL sensor shown in Figure 4-6 where the transmit beam is directed to the scene with a final 45° turn mirror attached to the back side of the telescope secondary (element 15). The biaxial geometry is important for detection of near-range targets in that it avoids the problem of return beam obscuration by the telescope secondary mirror. This was not an issue with the FAL system, because long range targets were of primary interest. In the case of the FAL sensor, the range where transmitted laser beam spreading was found to provide a significant return signal was on the order of 120 m; therefore, the FAL system is effectively blind for ranges less than this value. The MiniFAL design avoids this problem, but its biaxial design introduces the requirement for minor parallax correction; however, for a small aperture system of this type correction is easy to achieve.

The telescope itself is based on a common optical prescription, but the material used to make the primary mirror and the support structure will be required to be light in weight. The required weight reduction compared to conventional components can be achieved by two means. These approaches include straightforward lightweighting of metallic mirrors and the use of mirrors made from carbon-graphite composites. Metallic mirrors in the required weight range could probably be fabricated, but this would depend on structural analysis yet to be undertaken. Studies have shown that the use of composite materials is very promising, but their use in the present application would require proof that the correct mirror figure could be maintained. In the case of structural supports, the use of a graphite-epoxy composite is recommended because of the stiffness and resistance to thermal expansion that these materials offer.

4.2.3. Electronics

The laser and sensor electronics include the laser control and firing system, the detector bias supplies and preamplifiers, a power distribution section to convert the 12 Vdc input to the various required voltage forms, the data acquisition cards, and the data storage device. The laser control and firing system designs will be based on the FAL system. Fabrication of these components, however, will require easily obtained circuit miniaturization by standard techniques. The same comments apply to the detector bias supplies, preamplifiers, and the power distribution section.

The data acquisition and storage section, shown in Figure 4-9, will be based on circuit cards to be developed at Hughes. The digitizer will use the same design as employed with the FAL sensor. The data storage device will likely be a Type III PCMCIA hard disk with a capacity of at least 250 MB. Considering a 30 MHz sampling rate, it is estimated that the data storage rate for two channels (transmit and receive signals) would be 1 MB/km/min. At a range of 2 km, it would

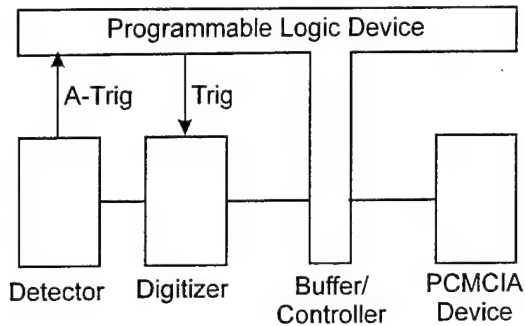


Figure 4-9. MiniFAL data acquisition system block diagram.

be possible to obtain data for a total elapsed time of two hours before replacement of the removable PCMCIA hard drive would be required. Note that there is no provision for data processing, although a modest capability could probably be included with a slight increase in system size. This possibility depends upon the extent and sophistication of the detection algorithm which is dictated by details of the mission scenario.

4.2.4. Weight analysis

A detailed weight analysis for the MiniFAL laser and integrated sensor designs was performed. In the case where presently available components were acceptable, their weights were determined by direct measurement. The weights of the remaining components that were anticipated to be the result of further development were determined by considering low risk designs and from material weights and standard fabrication techniques. These component issues are discussed in the following section. The MiniFAL laser and sensor weight analyses are summarized in Tables 4-5 and 4-6, respectively.

The laser weight analysis is tabulated in sections related to (1) the head composed of the pressure vessel and internal components; (2) the high voltage section; (3) optical assemblies; (4) the laser electronics composed of power distribution elements and the fire control section; and (5) the mechanical assemblies required to attach the laser to the sensor bench. Total weight for the complete laser is estimated to be 21 lb. All critical components have been qualified in prior laser designs. It remains to validate the efficacy of high speed gas flow in the compact design with regard to high repetition rate discharge operation, but experience with repetition rates up to 100 Hz suggests that the 30 Hz repetition rate of the MiniFAL should pose no problems. Finally, it should be noted that significant weight reduction compared to prior prototype designs is anticipated by the use of composite materials. These materials have been validated in the FAL design and are implementable in the MiniFAL design with low risk.

Table 4-5. MiniFAL laser weight analysis.

Item	Weight (lb)	Subtotal (lb)
<i>Head</i>		9.8
Pressure vessel/ flow system	5	
Disch module and top	4	
Ext fan motor	0.3	
Int fan motor	0.5	
<i>High V Section</i>		7.61
Capacitor	1.61	
Cap plates and potting	1	
Sparkgap	0.5	
Power supply	3	
Mounts	1	
Cables	0.2	
Coil	0.3	
<i>Optical assembly</i>		2.01
Optical bench	1.5	
Output coupler (2"dia.x0.2")	0.01	
Intracav beam expander	0.2	
Shifter	0.3	
<i>Laser Electronics</i>		0.8
Power/signal distribution	0.2	
Power supplies, trigger gen	0.2	
thermal controller	0.2	
Intracomponent cables	0.1	
Cooling fan	0.2	
<i>Supports</i>		0.2
Legs/attach	0.2	
Base		
Total		20.52

The sensor weight analysis is divided into sections related to (1) opto-mechanical components, (2) electronics, and (3) the data acquisition and storage sections. Total weight of the integrated sensor, including the laser, is estimated to be 33 lb. With respect to structural components, the designs depend on the use of stiff, lightweight materials, primarily carbon-graphite composites which pose no problem. The fabrication of optical components using this material has been demonstrated with small elements and its application to the MiniFAL requires further development. The electronic designs will achieve low weight and volume by use of high density circuit cards similar to prior designs developed and demonstrated at Hughes. The data acquisition and storage sections will make use of off-the-shelf, miniature computer cards that support standard data buses. Data storage will be through the use of widely available, compact PCMCIA components.

Table 4-6. MiniFAL sensor weight analysis.

Item	Weight (lb)	Subtotal (lb)	Comment
<i>Laser</i>		20.52	
<i>Opto-Mechanical</i>		5.1	
Telescope	1		
Cryoengine and detector	2		
Integrating sphere/Xmt det	0.3		
Beamsplitter	0.2		ZnSe
Transmit condenser lens	0.1		
Sensor housing	0.2		Carbon-graphite
Optical bench	0.7		Carbon-graphite
Monopod	0.2		Carbon-graphite
TV	0.4		
<i>Electronics</i>		7.56	
Transmit/receive preamps	0.2		
Power supplies	3		
Triggers	0.3		
Power distribution	1		12 Vdc input
<i>Data acquisition/storage</i>			
A-D card	0.2		2 chan
Microcomputer	0.4		Programmable
Micro interface adapter	0.2		Buffer controller
PCMCIA adapter	0.26		
PCMCIA hard drive	0.3		1 MB/km/min
Chassis and passive backplane	0.2		
Electronics housing	0.2		Compartmentalized
Interface	0.2		Key pad, readouts
Monitor	0.4		
GPS	0.2		
Cabling	0.5		
Total		33.18	

4.3. MINIFAL DEVELOPMENT

Development of the MiniFAL is anticipated to take place in three phases. The first phase will involve two parallel efforts to (1) validate the compact laser design and (2) develop laser and sensor critical components. The second phase will make use of the results of phase 1 in the development of the first prototype MiniFAL sensor. Phase 3 will have the objective of further device development to the point of deployment. This report deals only with the two tasks related to the first phase and the details of subsequent program phases are not discussed.

The laser and sensor designs outlined in the previous section are based on detailed analysis of existing components used in the Modular TEA laser and in FAL and on expectations of further development. Extensive experience in these areas suggests that this additional development can be accomplished with application of well known engineering approaches. The weight goal will be achieved by use of advanced materials and through careful attention to

component and system construction. For example, mechanical structures will be designed to serve multiple functions, such as providing rigidity for optical alignment retention combined with fixturing for multiple elements. Hughes has a great deal of experience in advanced designs using similar approaches and these have been proven in a number of laser and FLIR production programs. The specific tasks to be addressed in the first phase of development with regard to validation of the basic compact laser design and to the components that require validation are summarized in Table 4-7. All approaches are deemed to be low risk.

Table 4-7. Design validation and component development approaches.

Component	Development Approach
<u>Laser</u> High gas flow and rep rate Lightweight structures Air cooling system Composite optical bench Intracavity beam expander Wavelength shifter High voltage trigger module Power supply EMI control	Short turn radius gas directors, high flush factor, fan speed Carbon-graphite composite, common designs Tangential fan, brazed fin stock, common processes Repeat FAL design and validate Repeat FAL design and validate Develop compact, lightweight version, 100 Hz shift rate max Miniaturize existing design Use off-the-shelf component and harden Proven shielding, optical coupling, and filters
<u>Sensor</u> Telescope Control electronics Data acquisition Outer case Cryoengine	Tradeoff composite or lightweight aluminum materials Miniaturize existing circuits and adapt to cards Miniaturize existing circuit Composite materials, common processes Lightweight materials

5. ALGORITHM DEVELOPMENT

5.1. INTRODUCTION AND SUMMARY

Differential absorption LIDAR is a well established technology for estimating the CL of vapor materials using two closely spaced wavelengths. Although generalizations to more than two wavelengths have been made the approach has remained tied to the DIAL paradigm of computing the ratios of wavelength return pairs.⁴ The crucial assumption underlying two or few wavelength DIAL is that for sufficiently closely spaced wavelengths, the target reflectance and lidar system response should be approximately constant, and therefore ratioing of signal returns should remove these usually unknown parameters. This is often a valid assumption as shown by the success of DIAL in some cases. There are other important cases, however, for which the assumption of a wavelength independent background is not a good assumption and in those cases chemical detection is greatly impaired using the conventional two wavelength ratio approach. In particular, the recent progress in FAL development offers the possibility of rapidly tuning to more than 60 wavelengths across the entire CO₂ laser band (9.2-10.7 μm). This broadband coverage is dictated in certain practical situations where single or multiple chemicals must be detected in the presence of interfering species as in the case of a MiniFAL mission. For such extended wavelength scans, it is highly likely that the assumption of a spectrally uniform background will not apply invalidating the use of conventional algorithms. Even within the DIAL framework it is difficult to select the pairs to ratio, since wavelength selection is typically a computer-intensive nonlinear optimization that is very scenario dependent. Finally, although there are theoretical justifications for using ratioed data for two wavelength DIAL, generalization of the ratioing approach to more than two wavelengths results in suboptimal algorithms.

Because of the problems with prior algorithmic approaches stated above, a new multiwavelength detection and CL estimation algorithm for MiniFAL applications was developed. This new approach uses well established techniques of multivariate statistical inference theory, in particular the likelihood ratio test methodology is used to produce optimal estimators for CL and its uncertainty as well as detection algorithms for the presence of vapor. In addition to addressing the problem of broad wavelength coverage, the new method also optimizes noise reduction techniques. The major conceptual difficulty in constructing optimal algorithms that transcend the DIAL framework lies in separating the unknown background spectral signature from the transmission change induced by the vapor(s) of interest. The basic idea here is to construct models analogous to the standard DIAL model under the vapor absent hypothesis H_0 and the vapor present case H_1 . The detection algorithm then becomes a hypothesis test for whether the observed data best supports the H_0 or H_1 hypotheses. The unknown parameters in the models such as CL are estimated as a by-product of the test algorithm using the method of maximum likelihood. In this way, the likelihood ratio test methodology produces estimators for CL as well as a statistic for comparison with a threshold chosen to provide a given false alarm probability. The overall computational flow is illustrated in Figure 5-1.

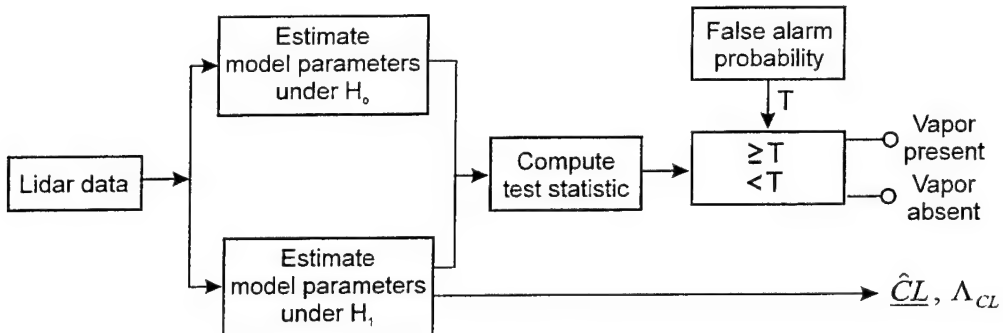


Figure 5-1. Algorithm computation flow diagram.

Since the statistical approach used here requires specific models for the data including noise under vapor present and absent conditions, three sets of assumptions about the nature of the spectral background have been analyzed, namely (1) a spectrally uniform background, (2) a background with a priori known relative spectral response, and (3) the case of arbitrary backgrounds for which a sample of data collected prior to the introduction of vapor is available. Clearly, the third situation is preferred when attainable, and the algorithms will be shown to provide better performance than the other cases. The uniform background model, while unlikely to be valid except in unusual situations, provides the most straightforward conceptual generalization of the DIAL approach. The second case may be of value for aerosol backscatter applications when it is possible to characterize the backscatter wavelength dependence in advance of the lidar measurement.

Derivations of the algorithm for the three model sets of assumptions are detailed below. For the case of range-resolved clouds, simulated data was used to verify the algorithms. For the case of CL measurement using returns from a hard target, actual lidar data was used. The data was collected with a FAL-based lidar operating against a hard target at about a 1 km range with a vapor chamber inserted into the path at approximately mid-range. The results clearly show the superiority of the new multiwavelength algorithm over the prior approach. The advantages of the new multiwavelength approach are that it:

- accounts for the noise aspects of the data to produce statistically optimal algorithms,
- accounts for the spectrally varying nature of the background,
- treats all wavelengths and multiple materials symmetrically and consistently,
- avoids pair-wise ratioing of data,
- generates closed-form detection and CL estimation equations,
- provides signal-to-noise ratio expressions for performance prediction,
- is based on a modeling framework that makes clear the assumptions and allows straightforward generalizations.

The first phase of algorithm development discussed in this report shows the superiority of the new approach. However, further work is required before the methodology can be applied to the general class of scenarios envisioned for the MiniFAL sensor. First, the aerosol algorithms that assumed range cell independence should be generalized to account for long laser transmitter pulses and correlated atmospheric volume backscatter. Second, prior temporal and range

correlation models of the vapor concentration should be introduced through a Bayesian approach that will lead to range smoothing and Kalman filtering of the *CL* data. Third, a sequential detection approach should be developed in lieu of the fixed sample method used here for achieving better detection power for small vapor releases. Finally, the unknown spectral background problem for time-varying vapor concentrations should be addressed by attempting to isolate the d.c. background by Fourier techniques. With the exception of the last rather speculative item, all these extensions have been investigated with respect to conventional algorithms and their application to the new MiniFAL algorithm should be straightforward.⁵⁻⁷

5.2. LIKELIHOOD RATIO TEST METHODOLOGY

Although well known in the statistics field, the use of optimal (likelihood ratio) tests may not be as familiar to the lidar community. For this reason, a short overview of the main ideas of importance to understanding the statistical tests to be considered below is presented. In common with all statistical inference, hypothesis testing is concerned with using data to choose between various classes of probability models as the "correct" description of events. For example, for topographic backscatter lidar the interest is in using lidar data collected over a set of N wavelength scans each having M wavelengths to decide whether the data are better represented by a model H_0 in which only ambient reflection and atmospheric extinction are present (together with detection and other noise), or whether a set of models collectively called H_1 is more appropriate in which one or more of a candidate set of Q vapor materials is partially absorbing the backscattered return.

It is traditional to specify the competing probability models by a family of probability distributions (or densities in the case of continuous data) $f(\mathbf{x}|\theta)$ in which $\mathbf{x} = [x_1, \dots, x_N]$ denotes the observed data vector, and $\theta = [\theta_1, \dots, \theta_k]$ denotes a set of parameters specifying the density. For an independent sample of data drawn from a univariate normal density, $\theta = [\theta_1, \theta_2]$ would represent the mean and variance and $f(\mathbf{x}|\theta)$ is

$$f(\mathbf{x}|\theta) = \prod_{i=1}^N \frac{1}{\sqrt{2\pi\theta_2}} \exp\left[-\frac{1}{2} \frac{(x_i - \theta_1)^2}{\theta_2}\right] \quad (1)$$

In the case of point estimation we would use the data \mathbf{x} to construct estimates of the parameters of the model θ via, for example, maximum likelihood (*ML*). In the case of hypothesis testing (detection) we are interested in using the data to infer which of a disjoint set of probability models H_i is best supported by the data. For example, in the case of the sample from the normal density (5.1) we may wish to decide whether the data came from a model H_0 with $\theta_1 = 0$ and $\theta_2 > 0$ but otherwise unknown, or from a model H_1 with $\theta_1 \neq 0$ and θ_2 positive and unknown. In this case, the parameter space $\Omega = \{(\theta_1, \theta_2): -\infty < \theta_1 < \infty, \theta_2 > 0\}$ becomes the disjoint union $\Omega = \Omega_0 \cup \Omega_1$ with $\Omega_0 = \{(\theta_1, \theta_2): \theta_1 = 0, \theta_2 > 0\}$ and $\Omega_1 = \{(\theta_1, \theta_2): \theta_1 \neq 0, \theta_2 > 0\}$. In this context, a hypothesis test is simply a rule for determining which sample values \mathbf{x} to associate each hypothesis H_i —that is, it is a partition of the sample space into disjoint subsets for which H_i will be accepted.

We note that in this simple example we are already confronting a test between composite hypotheses, since under H_0 , the variance θ_2 can be any positive number, whereas under H_1 , both θ_1 and θ_2 can vary continuously. In contrast to the simple hypothesis tests in which only a few discrete candidate probability models must be entertained, the test here must choose between two or more classes of models, each of which has a continuum of members. The likelihood ratio test was developed by Neyman and Pearson to treat such situations.⁸ We first observe that if Ω_0 and Ω_1 were discrete points instead of continuous regions of R^2 , the Neyman-Pearson lemma states that the test statistic

$$L(\mathbf{x}) = \frac{f(\mathbf{x}|\Omega_1)}{f(\mathbf{x}|\Omega_0)} \quad (2)$$

achieves the best performance of any possible test (i.e., has the highest detection power) in terms of maximizing the probability of correctly choosing H_1 given that H_1 is indeed true while guaranteeing that the size of the test—that is, the probability of choosing H_1 given H_0 —is no more than some fixed small number α .

The likelihood ratio test (LRT) statistic is found by replacing (2) with maximum likelihood parameter estimates of the parameter sets under each hypothesis

$$L(\mathbf{x}) = \frac{\max_{\theta \in \Omega_1} f(\mathbf{x}|\theta)}{\max_{\theta \in \Omega_0} f(\mathbf{x}|\theta)} \quad (3)$$

For technical reasons it is more convenient and mathematically equivalent to replace the maximization under H_1 over Ω_1 by maximization over the whole parameter space Ω —that is,

$$L(\mathbf{x}) = \frac{\max_{\theta \in \Omega} f(\mathbf{x}|\theta)}{\max_{\theta \in \Omega_0} f(\mathbf{x}|\theta)} \quad (4)$$

The resulting test bears the same relation to hypothesis testing as maximum likelihood estimation has to point estimation theory. It has intuitive appeal and often leads to tests that are UMP (uniformly most powerful) whenever such tests exist. In the normal density example given above, (4) leads to the Student t-test.

Although it is generally difficult to find closed form expressions for the distribution of L under H_0 and H_1 for finite sample cases, there is a well characterized large sample ($N \rightarrow \infty$) theory that leads to chi-squared distributions for the test statistic $I \equiv \ln L$; this asymptotic theory is usually adequate in practice as we show in Section 5.3.

5.3. ALGORITHM CONSTRUCTION

In this section we show how the LRT methodology outlined in Section 5.2 can be used to develop algorithms for detecting and estimating chemical vapors using the rapidly tunable laser sources now available. As indicated in the Introduction, it is useful to categorize the algorithms according to what is known (or at least assumed) about the target spectral background as well as

the type of target—that is, either topographic or aerosol. For each set of assumptions about the spectral background we characterize the detection and estimation algorithms through

- The statistical model assumptions about the data
- The maximum likelihood equations for the vector of path-integrated concentrations, \mathbf{CL} , derived as a by-product of the LRT development
- The associated expressions for the covariance of the \mathbf{CL} estimates
- The expression for the test statistic
- The asymptotic (large sample) distribution of the log-likelihood ratio test statistic.

The latter is needed for implementation of the test, either as a classical Neyman-Pearson threshold test or as a significance level (p -value) approach. Whenever appropriate the calculations are illustrated through simulated data examples.

5.3.1. Uniform spectral background

Topographic target

The case of a topographic backscatter target with assumed constant spectral reflectivity is the simplest and most direct generalization of the DIAL algorithm in that it assumes the mean spectral differences in the received signal are due entirely to absorption by the vapor(s) of interest. Although there may be situations such as backscatter from spectrally flat surfaces such as flame-sprayed aluminum for which this is a reasonable approximation, we consider it in detail primarily because it illustrates the LRT methodology without the computational details needed to address more realistic model assumptions.

Under the vapor absent hypothesis, H_0 , the backscatter data are represented simply as

$$P(i,j) = G + n(i,j) \quad (5)$$

where $1 \leq i \leq N$ denotes a set of wavelength scans at lidar wavelengths having indices $1 \leq j \leq M$, G denotes a constant but unknown mean lidar return signal from the topographic target, and $n(i,j)$ describes the zero-mean shot-to-shot fluctuation in the received signal due to a combination of speckle, atmospheric turbulence, beam jitter, and detector noise sources. We take n to be normally distributed and independent from scan to scan, but to have a generally non-diagonal covariance as a function of wavelength index

$$\Lambda_n(i,j,i',j') \equiv E n(i,j) n(i',j') = \Lambda(j,j') \delta_{ii'} \quad (6)$$

where $\delta_{ii'}$ is the Kronecker delta and Λ denotes the wavelength covariance (E denotes expectation). The unknown “constant” G is of course a function of range, target reflectivity, ambient atmospheric extinction, and lidar system parameters, but those dependencies are irrelevant in the present context. From the model assumptions above, the density of \mathbf{P} under H_0 is multivariate normal with mean G and block diagonal covariance $\Lambda \otimes I_N$, where \otimes denotes the Kronecker outer product and I_N is the N -dimensional identity matrix

$$f_0(\mathbf{P}|\mathbf{G}, \Lambda) = \prod_{i=1}^N (2\pi)^{-M/2} |\Lambda|^{-1/2} \exp \left[-\frac{1}{2} \sum_{j,j'=1}^M (P(i,j) - G) \Lambda^{-1}(j,j') (P(i,j') - G) \right] \quad (7)$$

where $|\Lambda|$ denotes the determinant of Λ .

Under the vapor-present hypothesis H_1 , the data are assumed to be given by a transmission-modulated version of (5):

$$P(i,j) = G \exp \left[-2 \sum_{l=1}^Q \rho_{jl} CL_l \right] + n(i,j) \quad (8)$$

where ρ_{jl} is the absorptivity of the l -th material at wavelength index j (taken to be known) and CL_l is the path-integrated concentration of vapor material l between the lidar and topographic target. The other parameters are the same as the H_0 model. In addition to G and Λ , the density of \mathbf{P} under H_1 depends on the unknown \mathbf{CL} vector giving

$$f_1(\mathbf{P}|G, \Lambda, \mathbf{CL}) = \prod_{i=1}^N (2\pi)^{-M/2} |\Lambda|^{-1/2} \exp \left[-\frac{1}{2} \sum_{j,j'=1}^M (P(i,j) - GT_j) \Lambda^{-1}(j,j') (P(i,j') - GT_{j'}) \right] \quad (9)$$

with

$$T_j(\mathbf{CL}) \equiv \exp \left[-2 \sum_{l=1}^Q \rho_{jl} CL_l \right] \quad (10)$$

the round-trip transmission factor. Following the prescription outlined in Section 5.2, the LRT statistic assumes the form

$$L = \frac{\max_{G, \Lambda, \mathbf{CL}} f_1(\mathbf{P}|G, \Lambda, \mathbf{CL})}{\max_{G, \Lambda} f_0(\mathbf{P}|G, \Lambda)} \quad (11)$$

or, since the logarithm is a monotone increasing function of its argument,

$$l \equiv \ln L = \max_{G, \Lambda, \mathbf{CL}} \ln f_1(\mathbf{P}|G, \Lambda, \mathbf{CL}) - \max_{G, \Lambda} \ln f_0(\mathbf{P}|G, \Lambda) . \quad (12)$$

Denoting by \hat{G}_0 and $\hat{\Lambda}_0$ the ML estimates of G and Λ under H_0 , computing the derivatives of $\ln f_0$ using (7) produces the result

$$\hat{G}_0 = \frac{1}{NM} \sum_{ij} P(i,j) \quad (13)$$

$$\hat{\Lambda}_0(j,j') = \frac{1}{N} \sum_{i=1}^N (P(i,j) - \hat{G}_0) (P(i,j') - \hat{G}_0) . \quad (14)$$

The corresponding maximizations of $\ln f_1$ for \hat{G}_1 , $\hat{\Lambda}_1$, and \bar{CL} produce the coupled set of equations

$$\hat{\Lambda}_1(j, j') = \frac{1}{N} \sum_{i=1}^N \left(P(i, j) - \hat{G}_1 \hat{T}_j \right) \left(P(i, j') - \hat{G}_1 \hat{T}_{j'} \right) \quad (15)$$

$$\hat{G}_1 = \frac{\sum_{j, j'} \hat{T}_j \hat{\Lambda}_1^{-1}(j, j') \bar{P}(j')}{\sum_{j, j'} \hat{T}_j \hat{\Lambda}_1^{-1}(j, j') \hat{T}_{j'}} \quad (16)$$

$$F_l(\hat{CL}) \equiv \sum_{j, j'} \hat{T}_j \hat{\Lambda}_1^{-1}(j, j') \bar{P}(j') \sum_{jj'} \rho_{jl} \hat{T}_j \hat{\Lambda}_1^{-1}(j, j') \hat{T}_{j'} - \sum_{j, j'} \rho_{jl} \hat{T}_j \hat{\Lambda}_1^{-1}(j, j') \bar{P}(j') \sum_{j, j'} \hat{T}_j \hat{\Lambda}_1^{-1}(j, j') \hat{T}_{j'} = 0 \quad (17)$$

with

$$\bar{P}(j) = \frac{1}{N} \sum_{i=1}^N P(i, j) \quad (18)$$

and

$$\hat{T}_j = \exp \left[-2 \sum_{l=1}^Q \rho_{jl} \hat{CL}_l \right]. \quad (19)$$

As these equations are nonlinear, iterative methods must be used to produce numerical solutions. The Newton-Raphson algorithm has worked well for solving the Q-dimensional equation set $\{F_l\}$ for CL; given an estimate $\bar{CL}_l^{(k)}$, a new estimate is constructed as

$$\hat{CL}_l^{(k+1)} = \hat{CL}_l^{(k)} - \sum_{l'=1}^Q H_{ll'}^{-1} F_{l'} \left(\hat{CL}^{(k)} \right), \quad (20)$$

where

$$H_{ll'} \left(\hat{CL}^{(k)} \right) \equiv \frac{\partial F_l \left(\hat{CL}^{(k)} \right)}{\partial \hat{CL}_{l'}}. \quad (21)$$

Starting with $\bar{CL}_l^{(0)} = 0$, $\bar{G}_1 = \bar{G}_0$, we compute \hat{T}_j , $\bar{\Lambda}_1$, \bar{G}_1 and $\bar{CL}_l^{(k+1)}$ and iterate until convergence. The resulting estimates for CL_l are the ML estimates obtained as a byproduct of the LRT approach.

The covariance of the CL estimates at convergence is obtained by computing the functional variation of F_l :

$$\delta F_l(CL) = \sum_{l'} H_{ll'} \delta CL_{l'} + \sum_j \frac{\partial F_l}{\partial \bar{P}(j)} \delta \bar{P}(j) = 0 \quad (22)$$

Solving for δCL_l gives

$$\delta CL_l = - \sum_{l'} H_{ll'}^{-1} \sum_j \frac{\partial F_{l'}}{\partial \bar{P}(j)} \delta \bar{P}(j) \quad (23)$$

and

$$\Lambda_{CL}^{\wedge}(l, l') = E \delta CL_l \delta CL_{l'} = \frac{1}{N} \sum_{l_1, l_2} H_{ll_1}^{-1} \sum_{j, j'} \frac{\partial F_{l_1}}{\partial \bar{P}(j)} \hat{\Lambda}_1(j, j') \frac{\partial F_{l_2}}{\partial \bar{P}(j')} H_{l'l_2}^{-1} \quad (24)$$

where

$$\frac{1}{N} \hat{\Lambda}_1(j, j') = E \delta \bar{P}(j) \delta \bar{P}(j')$$

was used.

Given the *ML* estimates of the model parameters under H_0 and H_1 , the log-likelihood ratio l in (12) becomes simply

$$l = \frac{N}{2} \ln \frac{|\hat{\Lambda}_0|}{|\hat{\Lambda}_1|} \quad (25)$$

with $\hat{\Lambda}_0$ and $\hat{\Lambda}_1$ given by (14) and (15).

Finally, the large-sample limiting distributions of $2l$ under H_0 and H_1 are chi-squared and non-central chi-squared, respectively. Because the details of their derivation are somewhat tedious, we only give the results here. The appendix has a sketch of the derivation. Under H_0 and H_1 for large N ,

$$f_0(l) \approx \frac{1}{\Gamma(Q/2)} l^{Q/2-1} e^{-l} \theta(l) , \quad (26)$$

$$f_1(l) \approx e^{-(\lambda^2/2+l)} \sum_{j=0}^{\infty} \frac{\lambda^{2j}}{2^j j!} \frac{l^{Q/2+j-1}}{\Gamma(Q/2+j)} \theta(l) , \quad (27)$$

where $\theta(l) = 1$, $l > 0$, $\theta(l) = 0$, $l \leq 0$, and λ^2 , the non-centrality parameter, plays the role of a generalized signal-to-noise ratio (snr) and is given by

$$\lambda^2 = N G^2 \sum_{j, j'} (T_j - \langle T \rangle) \Lambda^{-1}(j, j') (T_{j'} - \langle T \rangle) , \quad (28)$$

with

$$\langle T \rangle = M^{-1} \sum_{j=1}^M T_j . \quad (29)$$

The likelihood ratio test and associated CL estimation algorithm discussed here were programmed in double precision Microsoft FORTRAN for use in evaluating their performance on simulated lidar data made from the models (5) and (8). Figure 5-2 plots the model of the spectral absorptivity. It represents the wavelength dependence of $M = 10$ wavelengths of two hypothetical vapor materials. The units are arbitrary. The histogram-based density estimate of the detection statistic l computed from 1000 trials of synthetic data was made assuming a uniform spectral background with $G = 10$ and noise standard deviation of 1 for a mixture of two materials having $CL_1 = 0$ and $CL_2 = 0$ with wavelengths having the spectral absorptivity profiles in Figure 5-2. The number of averaged wavelength scans, N , was 100 for this example. Figure 5-3 shows a histogram of the CL estimates with fits to Gaussian densities having the estimated means and variances derived from the 1000 trials. The agreement in all cases is excellent.

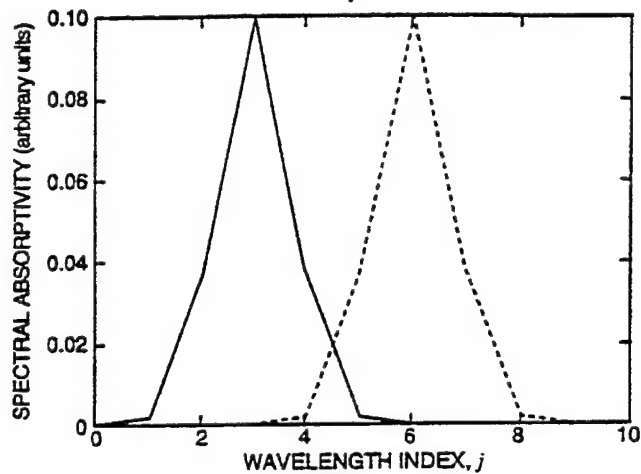


Figure 5-2. Hypothetical absorptivity vs wavelength.

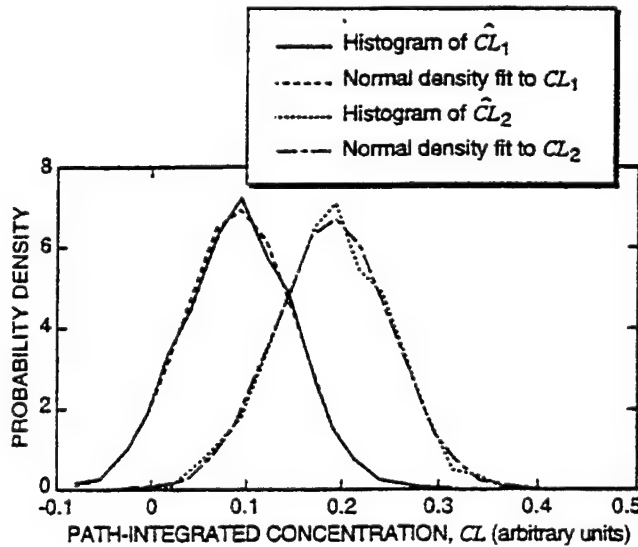


Figure 5-3. Estimated CL .

Aerosol target

Under the assumption of a short transmitter pulse and uncorrelated aerosol backscatter (as would be expected from a uniformly distributed aerosol), the model developed for topographic backscatter above becomes under H_0 ,

$$P(i,j,k) = G(k) + n(i,j,k) , \quad (30)$$

where $G(k)$ denotes the mean spectrally uniform backscatter at range cell k , $1 \leq k \leq Nr$, for $1 \leq i \leq N$ wavelength scans at $1 \leq j \leq M$ wavelengths. The noise term $n(i,j,k)$ is again taken to be zero-mean and normally distributed with range-diagonal covariance

$$\Lambda(i,j,k;i',j',k') = \Lambda_k(j,j')\delta_{kk'}\delta_{ii'} . \quad (31)$$

Here $\Lambda_k(j,j')$ denotes the generally non-diagonal wavelength covariance at range cell k . The corresponding data model under H_1 is

$$P(i,j,k) = G(k) \exp \left[-2 \sum_{l=1}^Q \rho_{jl} CL_l(k) \right] + n(i,j,k) , \quad (32)$$

where $CL_l(k)$ represents the path-integrated concentration of material l at the k -th range cell.

Due to the assumption of uncorrelated backscatter from different range cells, the detection and estimation equations are exactly those of the previous section at each range cell—that is, (13) and (14) become

$$\hat{G}_0(k) = \frac{1}{NM} \sum_{i=1}^N \sum_{j=1}^M P(i,j,k) \quad (33)$$

$$\hat{\Lambda}_{0k}(j,j') = \frac{1}{N} \sum_{i=1}^N (P(i,j,k) - \hat{G}_0(k)) (P(i,j',k) - \hat{G}_0(k)) . \quad (34)$$

Likewise, the *ML* estimation equations (17) for CL , $F_l(CL) = 0$, become $F_{kl}(CL(k)) = 0$, with corresponding changes to T_j , Λ_1 , and G_1 . The log-likelihood ratio statistic given by (25) for topographic backscatter generalizes to

$$l = \frac{N}{2} \sum_{k=1}^{Nr} \ln \frac{|\hat{\Lambda}_{0k}|}{|\hat{\Lambda}_{1k}|} . \quad (35)$$

Because the sum of independent chi-squared random variables (central or not) is again chi-squared, the asymptotic density for l becomes

$$f_0(l) = \frac{1}{\Gamma\left(\frac{NrQ}{2}\right)} l^{NrQ/2-1} e^{-l} \theta(l) \quad (36)$$

under H_0 , and

$$f_1(l) = \exp\left[-\left(l + \frac{1}{2} \sum_{k=1}^{Nr} \lambda_k^2\right)\right] \sum_{j=0}^{\infty} \frac{\left(\sum_k \lambda_k^2\right)^j}{2^j j!} \frac{l^{NrQ/2+j-1}}{\Gamma\left(\frac{NrQ}{2} + j\right)} \theta(l) \quad (37)$$

under H_1 , with the non-centrality parameter λ_k^2 representing the generalized snr from backscatter at range cell k :

$$\lambda_k^2 = NG^2 \sum_{j,j'} \left(T_j(k) - \langle T_k \rangle \right) \Lambda_k^{-1}(j,j') \left(T_{j'}(k) - \langle T_k \rangle \right), \quad (38)$$

with

$$\langle T_k \rangle = M^{-1} \sum_{j=1}^M T_j(k) \quad (39).$$

The aerosol target version of the uniform spectral backscatter model was programmed and evaluated on synthetic lidar data. Because of the qualitative similarity of the results of the simulation to those given in Section 5.3.2, we discuss the numerical results in that section.

5.3.2. Known spectral background

This section describes the detection and estimation algorithms that result from adopting the second set of model assumptions about the spectral background indicated in the Introduction; namely, the relative spectral response of the background is known but the overall amplitude that is a function of range, lidar parameters, and so on, is unknown. For simplicity, we consider the case of an aerosol target producing uncorrelated backscatter returns as a function of range cell as for the aerosol target above. The topographic case is easily obtained from the results here by taking only one range cell. Also, the assumption of prior spectral background shape is better suited to the aerosol or Mie scattering scenario than the topographic case.

The data model under H_0 becomes

$$P(i,j,k) = A_k g(j,k) + n(i,j,k), \quad (40)$$

where $g(j,k)$ represents the known or assumed spectral response of the atmosphere at wavelength index j , range cell k , A_k is the unknown amplitude of the received signal at cell k , and $n(i,j,k)$ is the additive noise contribution having the properties specified in Section 5.3.1. The prior term $g(j,k)$ is allowed to have a range cell as well as wavelength dependence to account for ambient range-dependent extinction; all other range dependent effects such as the $1/r^2$ signal dependence are modeled by A_k .

The probability density for \mathbf{P} under H_0 is parameterized by \mathbf{A} and Λ giving

$$f_0(\mathbf{P}|\mathbf{A}, \Lambda) = \prod_{i=1}^N \prod_{k=1}^{Nr} (2\pi)^{-M/2} |\Lambda_k|^{-1/2} \exp\left[-\frac{1}{2} \sum_{j,j'} \left(P(i,j,k) - A_k g(j,k) \right) \Lambda_k^{-1}(j,j') \left(P(i,j',k) - A_k g(j',k) \right) \right]. \quad (41)$$

The LRT approach generates the following ML estimates of \mathbf{A} and Λ under H_0 :

$$A_{0k} = \frac{\sum_{j,j'} g(j,k) \hat{\Lambda}_{0k}^{-1}(j,j') \bar{P}(j',k)}{\sum_{j,j'} g(j,k) \hat{\Lambda}_{0k}^{-1}(j,j') g(j',k)} \quad (42)$$

$$\hat{\Lambda}_{0k}(j,j) = \frac{1}{N} \sum_{i=1}^N \left(P(i,j,k) - \hat{A}_{0k} g(j,k) \right) \left(P(i,j',k) - \hat{A}_{0k} g(j',k) \right) \quad (43)$$

with

$$\bar{P}(j,k) \equiv \frac{1}{N} \sum_{i=1}^N P(i,j,k) \quad (44)$$

The corresponding data model under H_1 is then

$$P(i,j,k) = A_k g(j,k) T_{jk}(\mathbf{CL}) + n(i,j,k) \quad (45)$$

with

$$T_{jk}(\mathbf{CL}) \equiv \exp \left[-2 \sum_{l=1}^Q \rho_{jl} CL_l(k) \right] \quad (46)$$

the usual vapor transmission factor. The density of \mathbf{P} under H_1 is parameterized by \mathbf{CL} as well as by \mathbf{A} and Λ producing

$$f_1(\mathbf{P}|\mathbf{A}, \Lambda, \mathbf{CL}) = \prod_{i=1}^N \prod_{k=1}^{Nr} (2\pi)^{-M/2} |\Lambda_k|^{-1/2} \exp \left[-\frac{1}{2} \sum_{j,j'} \left(P(i,j,k) - A_k g(j,k) T_{jk} \right) \Lambda_k^{-1}(j,j') \left(P(i,j',k) - A_k g(j',k) T_{j'k} \right) \right]. \quad (47)$$

Applying the *ML* estimation procedure to $\ln f_1$ generates the coupled set of equations for \hat{A}_{1k} , $\hat{\Lambda}_1$, and \bar{CL} :

$$\hat{A}_{1k} = \frac{\sum_{j,j'} g(j,k) \hat{T}_{jk} \hat{\Lambda}_1^{-1}(j,j') \bar{P}(j',k)}{\sum_{j,j'} g(j,k) \hat{T}_{jk} \hat{\Lambda}_1^{-1}(j,j') g(j',k) \hat{T}_{j'k}} \quad (48)$$

$$\hat{\Lambda}_{1k}(j,j') = \frac{1}{N} \sum_{i=1}^N \left(P(i,j,k) - \hat{A}_{1k} g(j,k) \hat{T}_{jk} \right) \left(P(i,j',k) - \hat{A}_{1k} g(j',k) \hat{T}_{j'k} \right) \quad (49)$$

$$\begin{aligned} F_{kl}(\mathbf{CL}) = & \sum_{j,j'} g(j,k) \hat{T}_{jk} \hat{\Lambda}_1^{-1}(j,j') \bar{P}(j',k) \sum_{j,j'} \rho_{jl} g(j,k) \hat{T}_{jk} \Lambda_1^{-1}(j,j') g(j',k) \hat{T}_{j'k} \\ & - \sum_{j,j'} \rho_{jl} g(j,l) \hat{T}_{jk} \Lambda_1^{-1}(j,j') \bar{P}(j',k) \sum_{j,j'} g(j,k) \hat{T}_{jk} \Lambda_1^{-1}(j,j') g(j',k) \hat{T}_{j'k} = 0 \end{aligned} \quad (50)$$

As in Section 5.3.1, these equations can be solved by the Newton-Raphson algorithm initialized with $\bar{CL}_l = 0$, and $\hat{A}_{1k} = \hat{A}_{0k}$. Except for the need to perform the calculation independently for

each range cell k and the factors $g(j,k)$, all the results of 3.1.1 are carried over including the CL covariance equations. The log-likelihood ratio test statistic is again given by (35):

$$l = \frac{N}{2} \sum_{k=1}^{Nr} \ln \frac{|\hat{\Lambda}_{0k}|}{|\hat{\Lambda}_{1k}|} \quad (51)$$

with $\hat{\Lambda}_{0k}$ and $\hat{\Lambda}_{1k}$ now given by (3.37) and (3.43). The asymptotic densities for l under H_0 and H_1 are (38) and (39) with the snr parameter λ_k^2 now given by

$$\lambda_k^2 = N A_k^2 \sum_{j,j'} g(j,k) \left(T_j(k) - \langle T_k \rangle \right) \Lambda_k^{-1}(j,j') g(j',k) \left(T_{j'}(k) - \langle T_k \rangle \right), \quad (52)$$

with

$$\langle T_k \rangle = M^{-1} \sum_{j=1}^M T_j(k) \quad (53)$$

the wavelength-averaged transmission to range cell k .

Implementation of these algorithms is greatly facilitated by the approximation of uncorrelated range cells; other than obvious changes to accommodate the prior background factors, $g(j,k)$, the programs for *ML* estimation and detection are essentially those developed for the topographic target model in 5.3.1 with an outer loop over the range cell variable k . Figure 5-4 shows the log of every other wavelength synthetic lidar return versus range for aerosol target data modeled to have a linear spectral reflectivity dependence over 10 wavelengths together with randomly generated ambient atmospheric extinction. This background information, $g(j,k)$, was used to derive the likelihood ratio test statistic and the CL values versus range shown in Figure 5-5 for two materials with $CL_1 = 1$ and $CL_2 = 2$ represented as Gaussian clouds of width 10 m centered at 150 m and 100 m, respectively. The absorptivity coefficients are shown in Figure 5-2. The CL curves plot the estimates and their one-sigma uncertainty versus range.

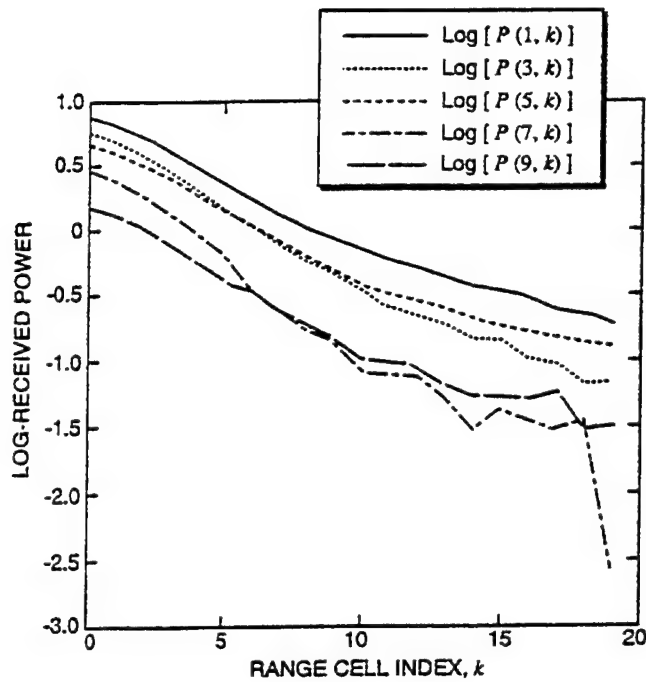


Figure 5-4. Synthetic data vs range bin.

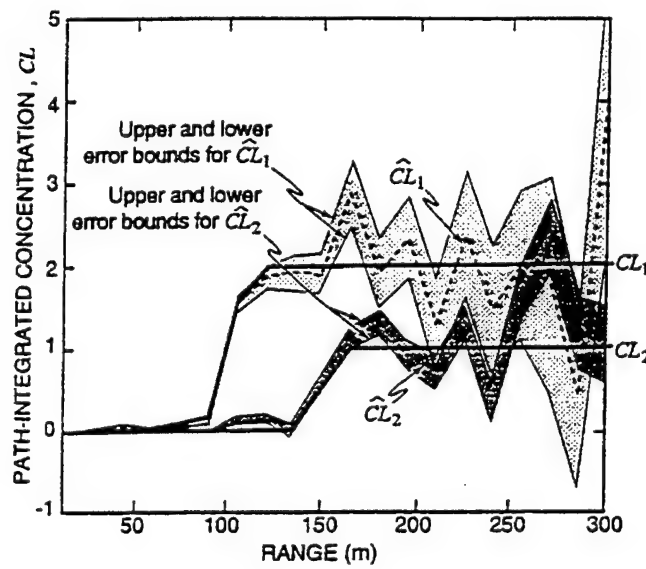


Figure 5-5. Estimated CL vs range.

5.3.3. Measured spectral background

In this section we analyze the third model set of assumptions, namely, the case for which a sample of N_0 scans of background data over the M wavelengths is collected prior to the

introduction of any of the Q target vapors. Although this case appears somewhat restrictive in comparison to the DIAL approach that theoretically does not require background data, we note that in practice background data are routinely used to normalize DIAL return signatures; the pure DIAL paradigm is rarely if ever used due to spectral bias even for closely spaced wavelengths. In any case, most fixed site monitoring applications are compatible with the use of background data. Here we explicitly treat the case of short-pulse aerosol backscatter lidar having a range-diagonal covariance matrix as with aerosol targets with a uniform spectral background and with the measured spectral background case. Also, topographic backscatter lidar is simply the restriction of the results here to a single range cell.

Prior to the introduction of target vapor materials, the data \mathbf{P} collected over $1 \leq i \leq N_0$ wavelength scans are modeled as

$$P(i, j, k) = G(j, k) + n(i, j, k) , \quad (54)$$

where $G(j, k)$ denotes the backscatter return at wavelength index j from the k -th range cell, and n is the additive zero-mean noise having covariance from aerosol target with uniform spectral background case.

$$\Lambda(i, j, k; i', j', k') = \Lambda_k(j, j') \delta_{ii'} \delta_{kk'} . \quad (55)$$

The N_0 scans are used to form the *ML* estimates of G and Λ as

$$\hat{G}(j, k) = \frac{1}{N_0} \sum_{i=1}^{N_0} P(i, j, k) \quad (56)$$

$$\hat{\Lambda}_k(j, j') = \frac{1}{N_0} \sum_{i=1}^{N_0} (P(i, j, k) - \hat{G}(j, k)) (P(i, j', k) - \hat{G}(j', k)) . \quad (57)$$

We assume N_0 can be chosen large enough that the estimates of G and Λ are of much smaller variance than those produced if the test data scans of length $N \ll N_0$ were used as in Sections 5.3.1 and 5.3.2.

The test data are now modeled as

$$P(i, j, k) \cong \hat{G}(j, k) + n(i, j, k) \quad (58)$$

under H_0 for N scans with the noise n having the approximate covariance $\hat{\Lambda}_k$ giving

$$f_0(\mathbf{P}) = \prod_{i=1}^N \prod_{k=1}^{Nr} (2\pi)^{-M/2} |\hat{\Lambda}_k|^{-1/2} \exp \left[-\frac{1}{2} \sum_{j, j'} (P(i, j, k) - \hat{G}(j, k)) \hat{\Lambda}_k^{-1}(j, j') (P(i, j', k) - \hat{G}(j', k)) \right] . \quad (59)$$

Under H_1 , the data model becomes

$$P(i, j, k) \cong \hat{G}(j, k) T_{jk}(\mathbf{CL}) + n(i, j, k) \quad (60)$$

with the transmission factor

$$T_{jk}(\mathbf{CL}) \equiv \exp \left[-2 \sum_{l=1}^Q \rho_{jl} CL_l(k) \right] \quad (61)$$

as before. The joint density for \mathbf{P} under H_1 is now parameterized by \mathbf{CL} as

$$f_1(\mathbf{P}|\mathbf{CL}) = \prod_{i=1}^N \prod_{k=1}^{Nr} (2\pi)^{-M/2} \left| \bar{\mathbf{A}}_k \right|^{-1/2} \exp \left[-\frac{1}{2} \sum_{j,j'} \left(P(i,j,k) - \bar{G}(j,k) T_{jk} \right) \bar{\mathbf{A}}_k^{-1}(j,j') \left(P(i,j',k) - \bar{G}(j',k) T_{j'k} \right) \right]. \quad (62)$$

As usual, the LRT methodology replaces the unknown parameters with their *ML* estimates; however, now H_0 is a simple hypothesis requiring no parameter estimation, and the alternative H_1 , while still composite, requires only the estimation of \mathbf{CL} . Differentiation of $\ln f_1$ leads to the score function set

$$F_{kl}(\hat{\mathbf{CL}}) = \sum_{j,j'} \rho_{jl} \hat{G}(j,k) \hat{T}_{jk} \hat{\Lambda}_k^{-1}(j,j') \bar{P}(j',k) - \sum_{j,j'} \rho_{jl} \hat{G}(j,k) \hat{T}_{jk} \hat{\Lambda}_k^{-1}(j,j') \hat{G}(j',k) \hat{T}_{j'k} = 0 \quad (63)$$

to be solved for $\bar{\mathbf{CL}}$ with

$$\bar{P}(j,k) = \frac{1}{N} \sum_{i=1}^N P(i,j,k) \quad (64)$$

$$\hat{T}_{jk} = \exp \left[-2 \sum_{l=1}^Q \rho_{jl} \hat{CL}_l(k) \right]. \quad (65)$$

Comparison of (63) with the coupled equation set (48)–(50) for the known spectral shape model shows that the use of background data provides an easier (although still nonlinear) optimization problem. The Newton-Raphson algorithm can be used to solve (63) via the iterations given by (20) with appropriate changes to H .

The CL covariance $\Lambda_{CL,k}(l,l')$ is given for each range cell k by

$$\Lambda_{\hat{CL}k}(l,l') = \frac{1}{N} \sum_{l_1, l_2} H_{ll_1}^{-1}(k) \sum_{j,j'} \frac{\partial F_{kl_1}}{\partial \bar{P}(j,k)} \hat{\Lambda}_k(j,j') \frac{\partial F_{kl_2}}{\partial \bar{P}(j',k)} H_{ll_2}^{-1}(k) \quad (66)$$

with $H_{ll'}(k) = \partial F_{kl}/\partial CL_l(k)$ and $\partial F_{kl}/\partial \bar{P}(j,k)$ computed from (63).

The log-likelihood ratio test statistic is found to be

$$l = \sum_{k=1}^{Nr} l_k \quad (67)$$

with

$$l_k = \frac{N}{2} \sum_{j,j'} \left(\bar{P}(j,k) - \bar{G}(j,k) \right) \bar{A}_k^{-1}(j,j') \left(\bar{P}(j',k) - \bar{G}(j',k) \right) \\ - \frac{N}{2} \sum_{j,j'} \left(\bar{P}(j,k) - \bar{G}(j,k) \bar{P}_{jk} \right) \bar{A}_k^{-1}(j,j') \left(\bar{P}(j',k) - \bar{G}(j',k) \bar{P}_{j'k} \right) \quad (68)$$

with \hat{T}_{jk} evaluated at the *ML* estimates of **CL**.

From the appendix we find the densities of l under H_0 and H_1 are asymptotically chi-squared and non-central chi-squared, respectively:

$$f_0(l) = \frac{l^{NrQ/2-1}}{\Gamma(NrQ/2)} e^{-l} \theta(l) \quad (69)$$

$$f_1(l) = \exp \left[- \left(l + \frac{1}{2} \sum_k \lambda_k^2 \right) \right] \sum_{j=0}^{\infty} \frac{\left(\sum_k \lambda_k^2 \right)^j}{2^j j!} \frac{l^{NrQ/2+j-1}}{\Gamma(NrQ/2+j)} \theta(l) \quad (70)$$

with the non-centrality parameter (signal-to-noise ratio) at range cell k

$$\lambda_k^2 = N \sum_{j,j'} G(j,k) (T_{jk} - 1) \Lambda_k^{-1}(j,j') G(j',k) (T_{j'k} - 1) \quad (71)$$

Specialization of the algorithm here to topographic backscatter lidar ($Nr = 1$) was applied to the same data used to generate Figure 5-3. The background spectral mean and covariance were estimated from $N_0 = 1000$ scans of background data; in practice, a much smaller number of scans would suffice. We note that although the probability versus log-likelihood plots for the uniform backscatter and measured backscatter models are nearly identical for $CL_1=CL_2=0$ as expected, the density for the test statistic l for the case of $CL_1=0.1$, $CL_2=0.2$ and a measured background has a mean value about twice that of the uniform background case. This improvement can be understood by comparing the snr expression in Eq. (71) with Eq. (38) or Eq. (52); they differ only in the replacement of the mean spectral transmission at range cell k $\langle T_k \rangle$ with simply one. This change, due to the use of prior background data, will provide higher power for the same test than the earlier models that are forced to estimate the background from vapor-containing data. This is the main reason for preferring to use background data whenever possible.

The detection and estimation algorithms using prior background data were also evaluated on vapor chamber data collected in the field.⁹ Data were collected for both single and multiple material injections using a number of toxic materials. Prior to the injection of vapor, a series of about $N_0=150$ wavelength scans using $M=32$ wavelengths was collected to provide the background spectral data. Subsequently, injections of 0.5 to 1, 2, 5, and 10 ml of vapor were made into the chamber at regular intervals and test data were collected. For this analysis $N=20$ test samples were used. The latter represents 10 s of data. The false alarm probability was chosen to be 0.01 per test data set of 20 scans.

The ML estimates of CL computed from Eq. 63) are shown in Figure 5-6 for the case of injection of MEK (methyl-ethyl-ketone) vapor. The times and amounts of injection are shown approximately. The $1-\sigma$ uncertainties computed from Eq. (66) are shown. The multiwavelength algorithms developed here responded to the lowest level of 1 ml; an earlier DIAL algorithm using Kalman filtering showed an erroneous decrease in concentration following the 1 ml injection.

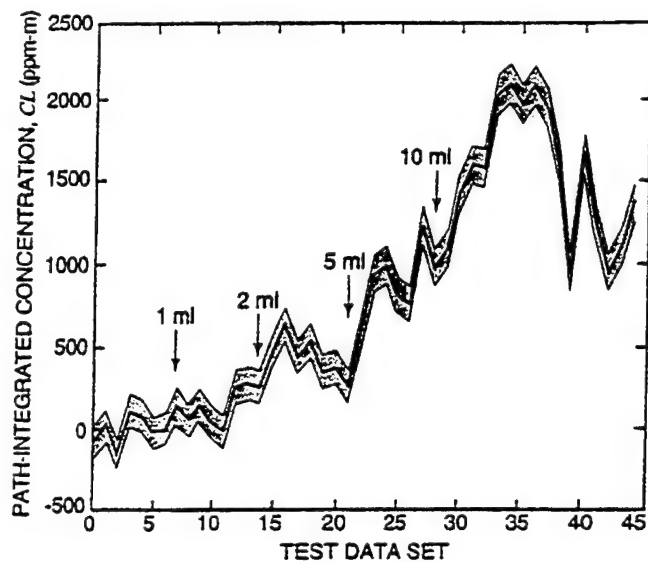


Figure 5-6. CL for MEK vs test data.

Figure 5-7 shows the analysis of a test involving three vapor materials injected at various times during the test: tetrachloroethane, tetrachloroethylene, and trichloroethane. The low CL values of tetrachloroethane are attributable to the very low (negative in some cases!) absorptivity estimates that were available. In general, the series shown parallels that given by the DIAL method. The results indicate the same basic approach using a fixed set of FAL wavelengths can operate in a multi-material setting.

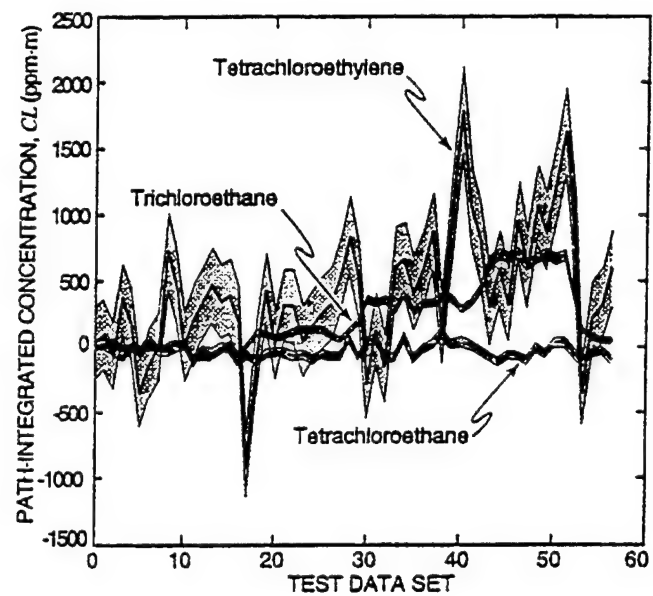


Figure 5-7. CL for three material injection.

6. WAVELENGTH SELECTION

The selection of laser transmitter wavelengths appropriate for detection depends critically upon the mission scenario and the needs of the detection algorithm. In the case that the single or multiple chemical species are known (in the presence of known interferences), the selection of wavelengths proceeds typically by choosing those that are at chemical absorption maxima and minima, assuming there is very little absorption spectrum overlap. In the event of significant spectral overlap, a larger number of lines would be required to map the shapes of the peaks in order to obtain chemical differentiation. Broadband scans are also required to eliminate wavelength-dependent background albedo effects. It was shown in Section 5 that an advanced algorithm could make optimal use of data from all laser lines whether at absorption maxima or not; therefore, it could be argued that as many lines as possible should be transmitted. However, target motion and evolution may prohibit the long data acquisition times required to obtain data from a large number of lines, in which case transmission of a few optimal lines would be recommended. The resolution of the question of how many lines to transmit, whether an entire band should be covered or whether a few selected lines would suffice, must be determined from analysis of actual field data.

In the absence of a fully developed algorithm to provide guidance and to make the process of wavelength selection tractable at this stage of scenario development, a selected list of chemicals was analyzed and only the wavelengths corresponding to the peaks and valleys of the absorption spectra were designated. Emission at the absorption peaks was considered to be an absolute requirement of the sensor. In that respect, it was found that some chemicals of interest did not have any absorption features in the typical wavelength range of the CO₂ laser. Of course, this was known from work in the FAL program. As a result of the FAL related problem, a program was initiated at Hughes to investigate techniques for shifting the wavelengths of the CO₂ laser. This investigation showed that wavelength shifting by a combination of second harmonic generation (SHG) and optical parametric oscillation (OPO) could provide access to all chemicals known to be of interest to the Army. Preliminary work on SHG and OPO has been reported in the literature for the separate processes and it remains to demonstrate the combined effect in a device that can be easily implemented in a chemical sensor. Discussion of this technique is outside the scope of this report, but it should be noted that methods to circumvent the CO₂ wavelength emission limitations have been identified that could be developed with relatively low risk.

The roster of chemicals that were analyzed is shown in Table 6-1. These can be divided into three categories. Category one contains chemicals recommended by Electronic Warfare Associates, Inc., such as SF₆ and MEK, appropriate for qualifying prototype sensors in the field. Category two includes chemicals that resulted from a study at Hughes and appear as precursors in drug and pesticide manufacturing or as industrial pollutants. Category three includes chemical warfare agents and these are shown for reference.

The various column designations of Table 6-1 are self-explanatory. Note that lines with a single asterisk have very poor atmospheric transmission over a 6 km path because of broadband

atmospheric absorption and these lines are probably not suitable for general use unless the path length is very short. Lines with a double asterisk would ordinarily be expected to have good atmospheric transmission but in fact transmission is poor because they lie at a narrow cleft in the transmission bands. These lines are also not recommended. The designation "Normal" in the column "Accessed By" indicates the standard bands of the normal isotope of CO₂. The designation "None" indicates that detection is not possible. SHG/OPO indicates wavelength shifting by the means described above. Triple means frequency tripling using techniques and crystals similar to the case of SHG/OPO.

Ammonia is an example of an easily detected chemical. In this case, the normal and relatively strong 10P34 and 10P20 CO₂ laser lines can be used. Acetone presents a case where detection can only be achieved by shifting the CO₂ laser lines to the 8.3 μm region. Fortunately this is the same wavelength needed to detect HD, mustard gas. Sulfur dioxide is an example of a chemical that cannot be readily detected at moderate to long range because of the poor atmospheric transmission of the laser line that can access the absorption peak at 8.6 μm . The range at which such a chemical could be detected would require further analysis.

Table 6-1. Sample chemicals and selected wavelengths.

Species	Detect	MW (amu)	Abs Peak (cm ⁻¹)	Abs Peak (μm)	Abs Coeff (10 ⁻⁴ m ² /mg)	Laser Line On	Laser Line Off	Accessed By ***	Application
Ammonia	Y	17	930.96	10.74	15.6	10P34	10P20	Normal	Phenom test
Carbon dioxide	N	44	2336.76	4.3	4.7	-	-	None	Coal power plant
Acetone	Y	58	2969.4	3.37**	0.47				Drug related
			1738.8	5.75*	2.36				
			1365.6	7.3*	1.52				
			1217.1	8.22	1.68				
2-Butanone (MEK)	Y	72.1	944.18	10.59	0.8	10P20	9P20	Normal	Industrial solvent
Sulfur dioxide	N	64	1360.78	7.34*	6.1	-	-	None	Coal, chem manuf
			1166	8.6**	0.47				
Sulfur hexafluoride	Y	146.1	949.22	10.54	30.2				Plume reference
			947.53	10.55	50.8				
			946.81	10.56	48.7				
Chloromethane	Y	50.5	1031.6	9.69	0.2	10P14	10R20	Normal	Normal
			1333	7.5*	0.48				
			2941	3.4	0.98				
Dichloromethane	Y	84.9	1266	7.9*	15				
			2941	3.4	2.3				
Trichloroethylene	Y	131.4	944.2	10.6	5.2				Pesticide manuf
Triethylphosphate (TEP)	Y	182.2	1043.16	9.59	10.6				Normal
Trimethylphosphite (TMP)	Y	124.1	1036.74	9.64	4.1				Plume reference
Ethyldiethanolamine	Y	133.2	1040.7	9.61	-	9P26	10P20	Normal	Precursor
Methyldiethanolamine	Y	119.2	1037.0	9.64	-	9P30	10P20	Normal	Precursor
Triethanolamine	Y	149.2	1036.5	9.65	-	9P30	10P20	Normal	Precursor
GA, Tabun	Y	162.3	1045.04	9.57	8.2	9P22	9P42	Normal	Agent
GB, Sarin	Y	140.1	1023.17	9.77	8.2	9P44	9P10	Normal	Agent
GD, Soman	Y	182.2	1023.17	9.77	9.4	9P44	9P10	Normal	Agent
HD, Distilled Mustard	Y	159.1	1037.44	9.64	0.22	9P30	9P6	Normal	Agent
			1204.82	8.3	1	Shifted	Shifted	SHG/OPO	

* Very poor atmospheric transmission

** Poor atmospheric transmission due to clefts

*** "Normal" indicates the standard bands of the normal isotope of CO₂

"None" indicates detection not possible

7. CONCLUSIONS AND RECOMMENDATIONS

The sensor analysis showed that either the direct or coherent detection approach could apply to certain scenarios. For the important case of range-resolved detection, however, analytical results based on the usual atmospheric backscatter coefficient suggested that the range with direct detection was very limited. Importantly, however, it was found that when the radar model was applied to an extrapolation from actual data with a direct detection system, the predicted range-resolved capability was greatly extended to 5 km. Results in the literature support this contention. The prevailing notion is that the backscatter coefficient for stack emissions is about a factor of 10^4 higher than the presumed atmospheric backscatter coefficient. Therefore, in the absence of conclusive field data for the particular chemicals of interest to the Army, it appears that sensors based on direct detection can be applied successfully to the detection of stack gas emissions. Verification of this scenario would require careful analysis of appropriate field data and in that regard application of the algorithm developed in this program to analysis of the data would be highly recommended.

The conceptual MiniFAL design developed in this program has a direct link to a prototype modular TEA laser developed under a prior Hughes IR&D program and the FAL laser and sensor development program with the Army. In that respect, the MiniFAL design is derived from a decade-long line of development of critical components, prototype laser heads, sensor systems, and field experience. The resulting MiniFAL conceptual design shows that a man-portable sensor could be developed with relatively low risk. This would require further development of certain components and subsystems and this development would draw upon existing components or components whose development would use well known engineering approaches and materials.

The first phase of algorithm development based on multivariate statistical inference theory reported here shows clear superiority to the conventional DIAL approach of using two-wavelength, ratioed data. This is borne out by the successful application of the new algorithm to both synthetic and actual field data. The new algorithm solves the crucial problem of variable background reflectivity as a function of wavelength that would be characteristic of the new FAL systems that offer rapid, broadband coverage. Broad band coverage is essential to the detection of single or multiple mixed chemicals in the presence of interfering species typical of practical scenarios. Furthermore, the natural adaptation of noise-reduction techniques to the new algorithm is a crucial attribute.

Further work is required before the new algorithm can be applied to the general class of scenarios envisioned for the MiniFAL sensor. First, the aerosol algorithms that assumed range cell independence should be generalized to account for long transmitter pulses and correlated atmospheric volume backscatter. Second, prior temporal and range correlation models of the vapor concentration should be introduced through a Bayesian approach that will lead to range smoothing and Kalman filtering of the CL data. Third, a sequential detection approach should be developed in lieu of the fixed sample method used here for achieving better detection power for small vapor releases. Fourth, the unknown spectral background problem for time-varying vapor

concentrations should be addressed by attempting to isolate the d.c background by Fourier techniques. With the exception of the last rather speculative item, all these extensions have been investigated with respect to conventional algorithms and their application to the new MiniFAL algorithm should be straightforward. Finally, coding is required for the FAL and projected MiniFAL systems in order to extract meaningful results from field test data.

A selected list of chemicals was analyzed and the wavelengths corresponding to the peaks and valleys of the absorption spectra were designated. Emission at the absorption peaks was considered to be an absolute requirement of the sensor. In that respect, it was found that some chemicals of interest did not have any absorption features in the typical wavelength range of the CO₂ laser. In order to solve this problem, it was suggested that certain techniques could be applied to wavelength shifting the TEA CO₂ laser so as to allow detection of all chemicals of interest to the Army. Investigation at Hughes of certain nonlinear effects in crystals has shown that the combined methods of SHG and OPO could be applied to achieve the required wavelength shifts. The embodiment of this technique in hardware for a chemical sensor would involve insertion in the transmit beam of a passive device composed of several crystals and beam directing optics. Insertion of the wavelength shift device would be a simple engineering task. Considering the importance of detecting certain chemicals that cannot now be detected with conventional lidars, it is strongly recommended that work in this area be continued.

REFERENCES

1. R. Lange, W. Diehl, M. Fiedler, E. Golusda, and K. Luhman, "Detection and localization of industrial pollutants with mobile CO₂-laser-based LIDAR", Proceedings, Optical Remote Sensing for Environmental and Process Monitoring, Sept 25-27, 1995, San Francisco, California.
2. D. B. Cohn, J. Fox, and C. Swim, "Wavelength agile laser and chemical sensor", SPIE vol. 2118 (1994).
3. J. A. Fox, C.R. Gautier, and J. L. Ahl, "Practical considerations for the design of CO₂ lidar systems", Appl. Opt. 27, 847 (1988).
4. R. E. Warren, "Detection and discrimination using multiple-wavelength differential absorption lidar", Appl. Opt. 24, 3541 (1985).
5. R. E. Warren, "Adaptive Kalman-Bucy filter for differential absorption lidar time series data", Appl. Opt. 26, 4755 (1987).
6. R. E. Warren, "Concentration estimation from differential absorption lidar using nonstationary Wiener filtering", Appl. Opt. 28, 5047 (1989).
7. S. M. Shannon and R. E. Warren, "Sequential detection of multiple materials using multiwavelength lidar time series data", Coherent Laser Radar: Technology and Applications, July 8-12, 1991, Snowmass, Colorado.
8. J. Neyman and E. S. Pearson, "On the use and interpretation of certain test criteria for purposes of statistical inference", Biometrika 20A, 175-240, 263-294 (1928).
9. L. Carr, C. Carlisle, D. Cooper, M. Crittenden, L. Fletcher, S. Gotoff, and F. Reyes, "Design and testing of a mobile vapor chamber for multiple material vapor analysis with a frequency-agile CO₂ DIAL system", Third Workshop on Standoff Detection for Chemical and Biological Defense, Williamsburg, Virginia (1994).